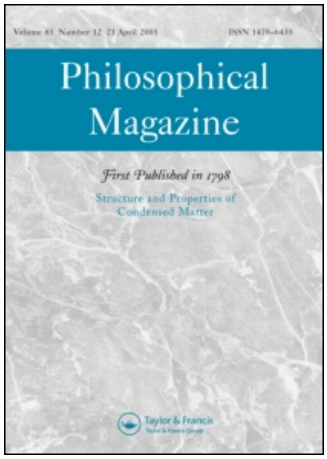

Philosophical Magazine
First published in 1798
Publication details, including instructions for authors and subscription information:
http://www.informaworld.com/smpp/title~content=t713695589

Self-consistent modelling of the mechanical behaviour of viscoplastic polycrystals incorporating intragranular field fluctuations

Online Publication Date: 01 October 2007
To cite this Article: Lebensohn, R. A., Tomé, C. N. and CastaÑeda, P. Ponte (2007) 'Self-consistent modelling of the mechanical behaviour of viscoplastic polycrystals incorporating intragranular field fluctuations', Philosophical Magazine, 87:28, 4287 - 4322
To link to this article: DOI: 10.1080/14786430701432619
URL: http://dx.doi.org/10.1080/14786430701432619

Philosophical Magazine,
Vol. 87, No. 28, 1 October 2007, 4287–4322

Self-consistent modelling of the mechanical behaviour of viscoplastic polycrystals incorporating intragranular field fluctuations

R. A. LEBENSOHN*†, C. N. TOMÉ† and P. PONTE CASTAÑEDA‡

†Los Alamos National Laboratory, Materials Science and Technology Division, Los Alamos, NM 87545, USA
‡Department of Mechanical Engineering and Applied Mechanics, University of Pennsylvania, Philadelphia, PA 19104-6315, USA

(*Received 9 March 2007; in final form 2 May 2007*)

We present a detailed description of the numerical implementation, within the widely used viscoplastic self-consistent (VPSC) code, of a rigorous second-order (SO) homogenization procedure for non-linear polycrystals. The method is based on a linearization scheme, making explicit use of the covariance of the fluctuations of the local fields in a certain linear comparison material, whose properties are, in turn, determined by means of a suitably designed variational principle. We discuss the differences between this second-order approach and several first-order self-consistent (SC) formulations (secant, tangent and affine approximations) by comparing their predictions with exact full-field solutions. We do so for crystals with different symmetries, as a function of anisotropy, number of independent slip systems and degree of non-linearity. In this comparison, the second-order estimates show the best overall agreement with the full-field solutions. Finally, the different SC approaches are applied to simulate texture evolution in two strongly heterogeneous systems and, in both cases, the SO formulation yields results in better agreement with experimental evidence than the first-order approximations. In the case of cold-rolling of low-SFE fcc polycrystals, the SO formulation predicts the formation of a texture with most of the characteristic features of a brass-type texture. In the case of polycrystalline ice, deforming in uniaxial compression to large strain, the SO predicts a substantial and persistent accommodation of deformation by basal slip, even when the basal poles become strongly aligned with the compression direction.

1. Introduction

The computation of the mechanical behaviour and the texture evolution of polycrystalline materials using self-consistent models is, nowadays, a standard approach in the Materials Science community. In 1987, Molinari *et al*. [1] developed the basic principles of the one-site viscoplastic (VP) self-consistent (SC) theory for polycrystal deformation. In 1993, Lebensohn and Tomé [2] numerically implemented this formulation to fully account for polycrystal anisotropy, developing the first

*Corresponding author. Email: lebenso@lanl.gov

Philosophical Magazine
ISSN 1478–6435 print/ISSN 1478–6443 online © 2007 Taylor & Francis
http://www.tandf.co.uk/journals
DOI: 10.1080/14786430701432619

version of the VPSC code. In the last decade, the VPSC code has experienced several improvements and extensions [3] and, nowadays, it is extensively used to simulate the plastic deformation of polycrystalline aggregates and to interpret experimental evidence on metallic, geological and polymeric materials.

Some of the applications of VPSC to metallic materials are: Zr-alloys (e.g. [2, 4–7]), Al-alloys (e.g. [8–13]), Cu-alloys (e.g. [14–16]), Ti-alloys (e.g. [17–19]), Mg-alloys (e.g. [20–23]), steels (e.g. [24–26]), Ni-alloys [27], U [28], Be [29], Ag [30], TiAl [31], Cu–Fe [32], Sn–Ag [33] and multilayered Cu–Nb [34]. Among the applications to geological materials, we can mention: ice (e.g. [35–37]), calcite [38], quartzite [39], halite [40], epsilon-iron [41, 42], olivine (e.g. [43–45]) and other Earth mantle's high-pressure phases, e.g. wadsleyite [46], ringwoodite [47, 48] and MgSiO3 perovskite [49], MgO magnesio-wüstite [49, 50] and SiO_2 stishovite [51]. In a recent application to polymeric materials, Nikolov *et al*. [52] adapted the VPSC code to study the mechanical behaviour of semicrystalline high-density polyethylene. Most of these applications were done using the tangent SC approximation described below.

In addition, VPSC has been improved to incorporate more complex deformation mechanisms, microstructures and processes. Worth mentioning are: modelling of deformation twinning (e.g. [2, 53]), modelling of dynamic recrystallization (e.g. [54]), solution of the inverse problem for identification of VPSC parameters [55], multiscale calculations coupling VPSC and Finite Element (FE) methods (e.g. [6, 10, 23, 44]), modeling of equal-channel extrusion (e.g. [56]), dilatational VPSC formulation for voided polycrystals [57], VPSC-based fitting of anisotropic yield functions to account for texture development and anisotropic hardening [58, 59]. The following multi-site extensions of the VPSC formulation have been proposed: two-site VPSC formulation [18], *n*-site VPSC formulation [60, 61] and VPSC formulation for lamellar structures [31].

The self-consistent approximation, one of the most commonly used homogenization methods to estimate the mechanical response behaviour of polycrystals, was originally proposed by Hershey [62] for linear elastic materials. For nonlinear aggregates (as those formed by grains deforming in the viscoplastic regime), the several self-consistent approximations proposed differ in the procedure used to linearize the non-linear local mechanical behaviour. Until now, the VPSC code offered the possibility of choosing among the *secant* (SEC) [63, 64], the *tangent* (TG) [1, 2] and the *affine* (AFF) [65] *first-order* SC approximations. All of them are based on linearization schemes at local level that make use of information on field averages only, disregarding higher-order statistical information inside the grains. However, the above assumption may be questionable (as first suggested by Gilormini's [66] systematic comparison between the different first-order SC approximations and bounds, for the case of two-phase non-linear composites), especially when strong directionality and large variations in local properties are to be expected. Such is the case for low rate-sensitivity materials, aggregates made of highly anisotropic grains, and multiphase polycrystals. In all those cases, strong deformation gradients are likely to develop inside grains owing to the contrast in properties between neighbouring grains. We show here that introducing intragranular fluctuations via higher-order statistical moments is particularly critical for the treatment of those materials and for the prediction of their mechanical behaviour and microstructural evolution.

To overcome the above limitations, Ponte Castañeda and coauthors have developed, over the last 15 years, more accurate nonlinear homogenization methods, using linearization schemes at grain level that also incorporate information on the second moments of the field fluctuations in the grains. These variational SC estimates are based on the use of so-called *linear comparison* methods, which express the effective potential of the nonlinear VP polycrystal in terms of a linearly viscous aggregate with properties that are determined from suitably designed variational principles. Two types of linear comparison estimates are available, depending on the linearization method used. The first method – known as the *variational* method – was originally proposed in 1991 for nonlinear composites [67], and then extended to VP polycrystals [68]. It makes use of the SC approximation for linearly viscous polycrystals to obtain bounds and estimates for nonlinear VP polycrystals. The second method – known as the *second-order* (SO) method – was proposed in 2002 for nonlinear composites [69] and later extended to VP polycrystals [70]. It makes use of the SC approximation for a more general class of linearly viscous polycrystals (i.e. those having a non-vanishing strain-rate at zero stress) to generate more accurate SC estimates for VP polycrystals, and derives its name from the fact that it leads to estimates that are exact to second-order in the heterogeneity contrast (as opposed to earlier methods, which are only exact to first-order in the contrast).

The 1991 variational formulation was applied to the study of the effective behaviour of cubic [71] and hexagonal [72] polycrystalline aggregates with fixed microstructure and to simulate texture evolution of hcp Ti at high temperature [73]. In the latter case, a better overall agreement was found with analogous FE simulations than corresponding Taylor and tangent SC predictions. The second-order SC formulation was used to generate estimates of the effective behaviour of random polycrystals and of the average field fluctuations in the constituent grains as a function of their orientation, in cubic and hexagonal materials [74], and to predict texture evolution in halite, an ionic cubic material [75]. In the latter case, the SO method predicts a pattern of texture evolution that was not captured by other homogenization methods, in good agreement with full-field FE predictions and experimental measurements. Finally, a thorough comparison between the different nonlinear SC estimates of the effective properties of cubic and hexagonal polycrystals [76] showed that the SO formulation yields the best overall agreement with corresponding ensemble averages of full-field results.

As a consequence, the implementation of a fully anisotropic SO approach inside VPSC is a necessary step towards improving its predictive capability for polycrystalline materials exhibiting high contrast in local properties. Unavoidably, this improved capability comes at the expense of algebraically more complex and numerically more demanding algorithms.

This paper describes in detail the implementation of the SO formulation inside the VPSC code [3]. The key aspect of this addition is the calculation of average field fluctuations inside the grains of the linear comparison polycrystal, in terms of the derivatives of the corresponding effective stress potential. It also shows examples in which improved predictions of the mechanical behaviour and microstructure evolution of polycrystals are obtained, when the fluctuations are accounted for in the homogenization procedure by means of the SO approach.

2. Viscoplastic self-consistent formalism

In this section, we first present the incompressible viscoplastic self-consistent formulation [77], using the affine linearization scheme [65]. Next, the methodology to calculate the average stress fluctuations in the grains of the linear comparison polycrystal is given and the second-order linearization procedure is described. Finally, algorithmic aspects of the SO implementation in VPSC are discussed.

In VPSC, the polycrystal is represented by means of weighted, ellipsoidal, statistically representative (SR) grains. Each of these SR grains represents the average behaviour of all the grains with a particular crystallographic orientation and morphology, but different environments. These SR grains should be regarded as representing the behaviour of *mechanical phases*, i.e. all the single crystals with a given orientation (r) belong to mechanical phase (r) and are represented by SR grain (r). (Note the difference between 'mechanical phases', which differ from each other only in terms of crystallographic orientation and/or morphology, and actual 'phases' differing from each other in crystallographic structure and/or composition). In what follows, 'SR grain (r)' and 'mechanical phase (r)' will be used interchangeably. The weights represent volume fractions. The latter are chosen to reproduce the initial texture of the material. In turn, each representative grain will be treated as an ellipsoidal viscoplastic inclusion embedded in an effective viscoplastic medium. Both, i.e. inclusion and medium, have fully anisotropic properties. Deformation is based on crystal plasticity mechanisms: slip and twinning systems activated by a resolved shear stress.

2.1. *Local constitutive behaviour and homogenization*

Let us consider a polycrystalline aggregate. The incompressible viscoplastic constitutive behaviour at each material point is described by means of the following non-linear, rate-sensitive equation:

$$\varepsilon(\overline{\mathbf{x}}) = \sum_k m^k(\overline{\mathbf{x}})\gamma^k(\overline{\mathbf{x}}) = \gamma_o \sum_k m^k(\overline{\mathbf{x}})\left(\frac{m^k(\overline{\mathbf{x}}) : \sigma(\overline{\mathbf{x}})}{\tau_o^s(\overline{\mathbf{x}})}\right)^n \tag{1}$$

In the above expression τ_o^k and $m_{ij}^k = (1/2)(n_i^k b_j^k + n_j^k b_i^k)$ are the threshold resolved shear stress and the symmetric Schmid tensor associated with slip (or twinning) system (k), where $\overline{\mathbf{n}}^k$ and $\overline{\mathbf{b}}^k$ are the normal and Burgers vector direction of such slip (or twinning) system, ε and σ are the deviatoric strain-rate and stress, and γ^k is the local shear-rate on slip (or twinning) system (k), which can be obtained as:

$$\gamma^k(\bar{\mathbf{x}}) = \gamma_o\left(\frac{m^k(\bar{\mathbf{x}}) : \sigma(\bar{\mathbf{x}})}{\tau_o^k(\bar{\mathbf{x}})}\right)^n \tag{2}$$

where γ_o is a normalization factor and n is the rate-sensitivity exponent. Let us assume that the following linear relation (i.e. an approximation of the actual non-linear relation, equation (1)) holds between the strain-rate and stress in the

SR grain (r):

$$\varepsilon(\overline{\mathbf{x}}) = M^{(r)} : \sigma(\overline{\mathbf{x}}) + \varepsilon^{o(r)} \tag{3}$$

where $M^{(r)}$ and $\varepsilon^{o(r)}$ are, respectively, the viscoplastic compliance and the back-extrapolated term of SR grain (r). Depending on the linearization assumption, $M^{(r)}$ and $\varepsilon^{o(r)}$ can be chosen differently (below we discuss some possible choices). Taking a volumetric average we obtain:

$$\varepsilon^{(r)} = M^{(r)} : \sigma^{(r)} + \varepsilon^{o(r)} \tag{4}$$

where $\varepsilon^{(r)}$ and $\sigma^{(r)}$ are average magnitudes in the volume of SR grain (r). Performing homogenization on a linear heterogeneous medium, whose local behaviour is described by equation (3), consists in assuming an analogous linear relation at the effective medium (macroscopic) level:

$$E = \bar{M} : \Sigma + E^o \tag{5}$$

where E and Σ are overall (macroscopic) magnitudes and $\bar{M}$ and E^o are the macroscopic viscoplastic compliance and back-extrapolated term, respectively. The latter moduli are *a priori* unknown and need to be adjusted. The usual procedure to obtain the homogenized response of a linear polycrystal is the linear self-consistent method. The problem underlying the self-consistent method is that of an inhomogeneous domain (r) of moduli $M^{(r)}$ and $\varepsilon^{o(r)}$, embedded in an infinite medium of moduli $\bar{M}$ and E^o. Invoking the concept of the equivalent inclusion [78], the local constitutive behaviour in domain (r) can be rewritten as:

$$\varepsilon(\overline{\mathbf{x}}) = \bar{M} : \sigma(\overline{\mathbf{x}}) + E^o + \varepsilon^*(\overline{\mathbf{x}}) \tag{6}$$

where $\varepsilon^*(\overline{\mathbf{x}})$ is an eigen-strain-rate field, which follows from replacing the inhomogeneity by an equivalent inclusion. Rearranging and subtracting (5) from (6) gives:

$$\tilde{\sigma}(\overline{\mathbf{x}}) = \bar{L} : (\tilde{\varepsilon}(\overline{\mathbf{x}}) - \varepsilon^*(\overline{\mathbf{x}})) \tag{7}$$

The symbol $\sim$ denotes local deviations from macroscopic values of the corresponding magnitudes and $\bar{L} = \bar{M}^{-1}$. Combining equation (7) with the equilibrium condition gives:

$$\sigma^c_{ij,j}(\overline{\mathbf{x}}) = \tilde{\sigma}^c_{ij,j}(\overline{\mathbf{x}}) = \tilde{\sigma}_{ij,j}(\overline{\mathbf{x}}) + \tilde{\sigma}^m_{,i}(\overline{\mathbf{x}}) \tag{8}$$

where σ^c_{ij} and σ^m are the Cauchy stress and the mean stress, respectively. Using the relation $\tilde{\varepsilon}_{ij}(\overline{\mathbf{x}}) = (1/2)\big(\tilde{u}_{i,j}(\overline{\mathbf{x}}) + \tilde{u}_{j,i}(\overline{\mathbf{x}})\big)$ between strain-rate and velocity-gradient, and adding the incompressibility condition associated with plastic deformation, we obtain:

$$\left| \begin{array}{l} \bar{L}_{ijkl}\tilde{u}_{k,lj}(\bar{\mathbf{x}}) + \tilde{\sigma}^m_{,i}(\bar{\mathbf{x}}) + f_i(\bar{\mathbf{x}}) = 0 \\ \tilde{u}_{k,k}(\bar{\mathbf{x}}) = 0 \end{array} \right. \tag{9}$$

where the fictitious volume force associated with the heterogeneity is:

$$f_i(\overline{\mathbf{x}}) = -\bar{L}_{ijkl}\varepsilon^*_{kl,j}(\overline{\mathbf{x}}) \tag{10}$$

System (9) consists of four differential equations with four unknowns: three are the components of velocity deviation vector $\tilde{u}_i(\overline{\mathbf{x}})$ and one is the mean stress deviation $\tilde{\sigma}^m(\overline{\mathbf{x}})$. Such system can be solved using the Green function method, as explained in Appendix A. The average strain-rate and rotation-rate in the equivalent inclusion (r) can be obtained from:

$$\tilde{\varepsilon}^{(r)} = S : \varepsilon^{*(r)} \tag{11}$$

$$\tilde{\omega}^{(r)} = \Pi : \varepsilon^{*(r)} = \Pi : S^{-1} : \tilde{\varepsilon}^{(r)} \tag{12}$$

where $\tilde{\varepsilon}^{(r)} = E - \varepsilon^{(r)}$ and $\tilde{\omega}^{(r)} = \Omega - \omega^{(r)}$ are deviations of the average strain-rate and rotation-rate inside the inclusion, with respect to the corresponding overall magnitudes, $\varepsilon^{*(r)}$ is the average eigen-strain-rate in the inclusion, and S and Π are the (viscoplastic) symmetric and skew-symmetric Eshelby tensors, functions of $\bar{L}$ and the shape of the ellipsoidal inclusion, representing the morphology of the SR grains.

2.2. *Interaction and localization equations*

Taking volume averages over the domain of the inclusion on both sides of equation (7) gives:

$$\tilde{\sigma}^{(r)} = \bar{L} : \left(\tilde{\varepsilon}^{(r)} - \varepsilon^{*(r)}\right) \tag{13}$$

Replacing the eigen-strain-rate given by equation (11) into equation (13), we obtain the *interaction equation*:

$$\tilde{\varepsilon}^{(r)} = -\tilde{M} : \tilde{\sigma}^{(r)} \tag{14}$$

where the interaction tensor is given by:

$$\tilde{M} = (I - S)^{-1} : S : \bar{M} \tag{15}$$

Replacing the constitutive relations for inclusion and effective medium in the interaction equation (14), after some manipulation one can write the following *localization equation*:

$$\sigma^{(r)} = B^{(r)} : \Sigma + b^{(r)} \tag{16}$$

where the localization tensors are defined as:

$$B^{(r)} = \left(M^{(r)} + \tilde{M}\right)^{-1} : \left(\bar{M} + \tilde{M}\right) \tag{17}$$

$$b^{(r)} = \left(M^{(r)} + \tilde{M}\right)^{-1} : \left(E^o - \varepsilon^{o(r)}\right) \tag{18}$$

2.3. *Self-consistent equations*

The derivation presented in the previous sections solves the problem of an equivalent inclusion embedded in an effective medium subjected to external loading conditions. In this section, we use the previous result to construct a polycrystal model, consisting

in regarding each SR grain (r) as an inclusion embedded in an effective medium that represents the polycrystal. The properties of such medium are not known *a priori* but have to be found through an iterative procedure. Replacing the stress localization equation (16) in the average local constitutive equation (4), we obtain:

$$\varepsilon^{(r)} = M^{(r)} : \sigma^{(r)} + \varepsilon^{o(r)} = M^{(r)} : B^{(r)} : \Sigma + M^{(r)} : b^{(r)} + \varepsilon^{o(r)} \tag{19}$$

Taking equation (19), enforcing the condition that the weighted average of the strain-rates over the aggregate has to coincide with the macroscopic quantities, i.e.:

$$E = \left\langle \varepsilon^{(r)} \right\rangle \tag{20}$$

(where the brackets $\langle\ \rangle$ denote average over the SR grains, weighted by the associated volume fraction), and using the macroscopic constitutive equation (5), we obtain the following *self-consistent equations* for the homogeneous compliance, and the back-extrapolated term (strain-rate at zero stress):

$$\bar{M} = \left\langle M^{(r)} : B^{(r)} \right\rangle \tag{21}$$

$$E^{o} = \left\langle M^{(r)} : b^{(r)} + \varepsilon^{o(r)} \right\rangle \tag{22}$$

These self-consistent equations are derived imposing the average of the local strain-rates to coincide with the applied macroscopic strain-rate (equation (20)). If all the SR grains are represented by ellipsoids that have the same shape and orientation, it can be shown that the same equations are obtained from the condition that the average of the local stresses coincides with the macroscopic stress. If the SR grains have different morphologies, they have associated different Eshelby tensors and the interaction tensors cannot be factored from the averages. In such a case, the following generalized self-consistent expressions should be used [79]:

$$\bar{M} = \left\langle M^{(r)} : B^{(r)} \right\rangle : \left\langle B^{(r)} \right\rangle^{-1} \tag{23}$$

$$E^{o} = \left\langle M^{(r)} : b^{(r)} + \varepsilon^{o(r)} \right\rangle - \left\langle M^{(r)} : B^{(r)} \right\rangle : \left\langle B^{(r)} \right\rangle^{-1} : \left\langle b^{(r)} \right\rangle \tag{24}$$

The self-consistent relations (21) and (22) are a particular case of (23) and (24). Both sets constitute fix-point equations that provide improved estimates of $\bar{M}$ and E^{o}, when they are solved iteratively starting from a suitable initial guess. From a numerical point of view, equations (23) and (24) are more robust and improve the speed and stability of the convergence procedure, even when solving a problem where all the inclusions have the same shape.

2.4. *Secant, affine, tangent and intermediate approximations*

As stated earlier, different choices are possible for the linearized behaviour at grain level and the results of the homogenization scheme depend on this choice. In what follows, we present several first-order linearization schemes, defined in terms of the stress first-order moment (average) inside SR grain (r).

The *secant approximation* [63, 64] consists in assuming the following linearized moduli:

$$M_{\text{sec}}^{(r)} = \gamma_o \sum_k \frac{m^{k(r)} \otimes m^{k(r)}}{\tau_o^{k(r)}} \left(\frac{m^{k(r)} : \sigma^{(r)}}{\tau_o^{k(r)}} \right)^{n-1} \tag{25}$$

$$\varepsilon_{\text{sec}}^{o(r)} = 0 \tag{26}$$

where the index (r) in $m^{k(r)}$ and $\tau_o^{k(r)}$ indicates uniform (average) values of these magnitudes, corresponding to a given orientation and hardening state associated with SR grain (r).

Under the *affine approximation* [65], the moduli are given by:

$$M_{aff}^{(r)} = n\gamma_o \sum_k \frac{m^{k(r)} \otimes m^{k(r)}}{\tau_o^{k(r)}} \left(\frac{m^{k(r)} : \sigma^{(r)}}{\tau_o^{k(r)}} \right)^{n-1} \tag{27}$$

$$\varepsilon_{aff}^{o(r)} = (1-n)\gamma_o \sum_k \left(\frac{m^{k(r)} : \sigma^{(r)}}{\tau_o^{k(r)}} \right)^{n} \tag{28}$$

In the case of the *tangent approximation* [1, 2], the moduli are, formally, the same as in the affine case: $M_{tg}^{(r)} = M_{aff}^{(r)}$ and $\varepsilon_{tg}^{o(r)} = \varepsilon_{aff}^{o(r)}$. However, instead of using these moduli and to avoid the iterative adjustment of the macroscopic back-extrapolated term, Molinari *et al.* [1] used the secant SC moduli (equations (25) and (26)) to adjust $\bar{M}$ (to be denoted $\bar{M}_{\text{sec}}$), in combination with the tangent–secant relation: $\bar{M}_{tg} = n\bar{M}_{\text{sec}}$ derived by Hutchinson [64]. Then, the expression of the interaction tensor is given by:

$$\tilde{M} = (I - S)^{-1} : S : \bar{M}_{tg} = n(I - S)^{-1} : S : \bar{M}_{\text{sec}} \tag{29}$$

Qualitatively, the interaction equation (14) indicates that the larger the interaction tensor, the smaller the deviation of grain stresses with respect to the average stress should be. As a consequence, for $n \to \infty$ the tangent approximation tends to a uniform stress state (*Sachs* or *lower-bound approximation*). This rate-insensitive limit of the tangent formulation is an artefact created by the use of the above tangent–secant relation of the non-linear polycrystal in the self-consistent solution of the linear comparison polycrystal. Since, on the other hand, the secant interaction has been proven to be stiff and to tend to a uniform strain-rate state (*Taylor* or *upper-bound approximation*) in the rate-insensitive limit, an *effective-n approximation* was proposed [80, 81]. This approximation gives a polycrystal response in between the stiff secant and the compliant tangent, which remains intermediate with respect to the bounds in the rate-insensitive limit and is obtained by replacing, in equation (29), the factor n by a 'tunable' parameter n^{eff}, chosen to be $1 < n^{eff} < n$. The interaction tensor is, therefore, given by:

$$\tilde{M} = n^{eff}(I - S)^{-1} : S : \bar{M}_{\text{sec}} \tag{30}$$

2.5. *Second-order formulation*

2.5.1. Second-order moments. The effective stress potential $\bar{U}_T$ of a linearly viscous polycrystal described by equation (5) may be written in the form [82, 83]:

$$\bar{U}_T = \frac{1}{2}\bar{M} :: (\Sigma \otimes \Sigma) + E^o : \Sigma + \frac{1}{2}\bar{G} \tag{31}$$

where $\bar{G}$ is the energy under zero applied stress. Let us rewrite the self-consistent expression for $\bar{M}$ and E^o (equations (21) and (22)) as:

$$\bar{M} = \left\langle M^{(r)} : B^{(r)} \right\rangle = \sum_r c^{(r)} M^{(r)} : B^{(r)} \tag{32}$$

$$E^o = \left\langle M^{(r)} : b^{(r)} + \varepsilon^{o(r)} \right\rangle = \sum_r c^{(r)} \left(M^{(r)} : b^{(r)} + \varepsilon^{o(r)} \right) = \sum_r c^{(r)} \varepsilon^{o(r)} : B^{(r)} \tag{33}$$

where $c^{(r)}$ is the volume fraction associated with SR grain (r). (The equivalence between both sums in equation (33) was proved by Laws [82]). Finally, the corresponding expression for $\bar{G}$ is:

$$\bar{G} = \sum_r c^{(r)} \varepsilon^{o(r)} : b^{(r)} \tag{34}$$

The average second-order moment of the stress field over a SR grain (r) of this polycrystal is a fourth-rank tensor given by [70]:

$$\langle \sigma \otimes \sigma \rangle^{(r)} = \frac{2}{c^{(r)}} \frac{\partial \bar{U}_T}{\partial M^{(r)}} \tag{35}$$

Replacing equations (31)–(34) in (35) we obtain:

$$\langle \sigma \otimes \sigma \rangle^{(r)} = \frac{1}{c^{(r)}} \frac{\partial \bar{M}}{\partial M^{(r)}} :: (\Sigma \otimes \Sigma) + \frac{1}{c^{(r)}} \frac{\partial E^o}{\partial M^{(r)}} : \Sigma + \frac{1}{c^{(r)}} \frac{\partial \bar{G}}{\partial M^{(r)}} \tag{36}$$

Using matrix notation for symmetric deviatoric tensors [84], the first derivative in the right term can be obtained solving the following equation:

$$\Omega_{ijkl} \frac{\partial \bar{M}_{kl}}{\partial M^{(r)}_{uv}} = \pi^{(r,uv)}_{ij} \tag{37}$$

where i, j, k, l and $u,v = 1,5$. The expressions for Ω_{ijkl} and $\pi^{(r,uv)}_{ij}$ are given in Appendix B. Expression (37) is a linear system of 25 equations with 25 unknowns (i.e. the components of $\partial \bar{M}_{kl}/\partial M^{(r)}_{uv}$). In turn, the other two derivatives appearing in equation (36) can be calculated as:

$$\frac{\partial E^o_i}{\partial M^{(r)}_{uv}} = \zeta_{ikl} \frac{\partial \bar{M}_{kl}}{\partial M^{(r)}_{uv}} + \kappa_i^{(r,uv)} \tag{38}$$

$$\frac{\partial \bar{G}}{\partial M^{(r)}_{uv}} = \varphi_{ij} \frac{\partial \bar{M}_{ij}}{\partial M^{(r)}_{uv}} + \vartheta_i \frac{\partial E^o_i}{\partial M^{(r)}_{uv}} + \eta^{(r,uv)} \tag{39}$$

where ξ_{ikl}, φ_{ij}, ϑ_i, $\kappa_i^{(r,uv)}$and $\eta^{(r,uv)}$ are given in Appendix B.

Once the average second moments of the stress are obtained, the corresponding second moments of the strain-rate can be calculated as:

$$\langle \varepsilon \otimes \varepsilon \rangle^{(r)} = \left(M^{(r)} \otimes M^{(r)} \right) :: \langle \sigma \otimes \sigma \rangle^{(r)} + \varepsilon^{(r)} \otimes \varepsilon^{o(r)} + \varepsilon^{o(r)} \otimes \varepsilon^{(r)} - \varepsilon^{o(r)} \otimes \varepsilon^{o(r)} \quad (40)$$

The average second moments can be used, for instance, to generate the average second moment of the equivalent stress and strain-rate in mechanical phase (r) as:

$$\bar{\bar{\sigma}}_{eq}^{(r)} = \left(\frac{3}{2} I :: \langle \sigma \otimes \sigma \rangle^{(r)} \right)^{1/2} \quad (41)$$

$$\bar{\bar{\varepsilon}}_{eq}^{(r)} = \left(\frac{2}{3} I :: \langle \varepsilon \otimes \varepsilon \rangle^{(r)} \right)^{1/2} \quad (42)$$

where I is the fourth order identity tensor. The standard deviations of the equivalent magnitudes over the whole polycrystal are defined as:

$$\mathrm{SD}(\sigma_{eq}) = \sqrt{\bar{\bar{\Sigma}}_{eq}^2 - \Sigma_{eq}^2} \quad (43)$$

$$\mathrm{SD}(\varepsilon_{eq}) = \sqrt{\bar{\bar{E}}_{eq}^2 - E_{eq}^2} \quad (44)$$

where:

$$\bar{\bar{\Sigma}}_{eq}^2 = \left\langle \left(\bar{\bar{\sigma}}_{eq}^{(r)} \right)^2 \right\rangle = \sum_r c^{(r)} \left(\bar{\bar{\sigma}}_{eq}^{(r)} \right)^2 \quad (45)$$

$$\bar{\bar{E}}_{eq}^2 = \left\langle \left(\bar{\bar{\varepsilon}}_{eq}^{(r)} \right)^2 \right\rangle = \sum_r c^{(r)} \left(\bar{\bar{\varepsilon}}_{eq}^{(r)} \right)^2 \quad (46)$$

The overall SDs defined by equations (43) and (44) are global scalar indicators that contain information about both inter-phase and intra-phase stress and strain-rate heterogeneity. Let us define alternate SDs that only reflects inter-phase (but not intra-phase) dispersions:

$$\mathrm{SD}'(\sigma_{eq}) = \sqrt{\left\langle \left(\sigma_{eq}^{(r)} \right)^2 \right\rangle - \Sigma_{eq}^2} \quad (47)$$

$$\mathrm{SD}'(\varepsilon_{eq}) = \sqrt{\left\langle \left(\varepsilon_{eq}^{(r)} \right)^2 \right\rangle - E_{eq}^2} \quad (48)$$

Finally, a measure of the intra-phase strain-rate heterogeneity relative to the total strain-rate heterogeneity can be defined as:

$$\delta\varepsilon_{\mathrm{intra}}^{\%} = \left(1 - \sqrt{\frac{\left\langle \left(\varepsilon_{eq}^{(r)} \right)^2 \right\rangle - E_{eq}^2}{\bar{\bar{E}}_{eq}^2 - E_{eq}^2}} \right) \times 100 \quad (49)$$

The latter adopts values between 0%, when the strain-rate is homogeneous inside each mechanical phase, i.e. $\langle(\varepsilon_{eq}^{(r)})^2\rangle = E_{eq}^2$, and 100%, when all the heterogeneity is due to fluctuations between mechanical phases, i.e. $\langle(\varepsilon_{eq}^{(r)})^2\rangle = \bar{\bar{E}}_{eq}^2$. An analogous magnitude can be defined for the intra-phase stress heterogeneity.

2.5.2. Second-order procedure. Once the average second-order moments of the stress field over each SR grain (r) are obtained by means of the calculation of the derivatives appearing in equation (36), the implementation of the SO procedure follows the work of Liu and Ponte Castañeda [70]. The covariance tensor of stress fluctuations is given by:

$$C_\sigma^{(r)} = \langle \sigma \otimes \sigma \rangle^{(r)} - \sigma^{(r)} \otimes \sigma^{(r)} \tag{50}$$

The average and the average fluctuation of resolved shear stress on slip system (k) of SR grain (r) is given by:

$$\bar{\tau}^{k(r)} = m^{k(r)} : \sigma^{(r)} \tag{51}$$

$$\hat{\tau}^{k(r)} = \bar{\tau}^{k(r)} \pm \left(m^{k(r)} : C_\sigma^{(r)} : m^{k(r)}\right)^{1/2} \tag{52}$$

where the positive (negative) branch should be selected if $\bar{\tau}^{k(r)}$ is positive (negative). The slip potential of slip system (k) is defined as:

$$\phi^k(\tau) = \frac{\tau_o^k}{n+1}\left(\frac{|\tau|}{\tau_o^k}\right)^{n+1} \tag{53}$$

Two scalar magnitudes associated with each slip system (k) of each SR grain (r) are defined by:

$$\alpha^{k(r)} = \frac{\phi'^{k(r)}\left(\hat{\tau}^{k(r)}\right) - \phi'^{k(r)}\left(\bar{\tau}^{k(r)}\right)}{\hat{\tau}^{k(r)} - \bar{\tau}^{k(r)}} \tag{54}$$

$$e^{k(r)} = \phi'^{k(r)}\left(\bar{\tau}^{k(r)}\right) - \alpha^{k(r)}\bar{\tau}^{k(r)} \tag{55}$$

where $\phi'^k(\tau) = \mathrm{d}\phi^k/\mathrm{d}\tau(\tau)$. The linearized local behaviour associated with SR grain (r) is then given by:

$$\varepsilon^{(r)} = M_{\mathrm{SO}}^{(r)} : \sigma^{(r)} + \varepsilon_{\mathrm{SO}}^{o(r)} \tag{56}$$

with:

$$M_{\mathrm{SO}}^{(r)} = \sum_k \alpha^{k(r)}\left(m^{k(r)} \otimes m^{k(r)}\right) \tag{57}$$

$$\varepsilon_{\mathrm{SO}}^{o(r)} = \sum_k e^{k(r)} m^{k(r)} \tag{58}$$

Once the linear comparison polycrystal is defined by equations (57) and (58) different second-order estimates of the effective behaviour of the nonlinear aggregate can be obtained. Approximating the potential of the nonlinear polycrystal in terms of the potential of the linear comparison polycrystal and a suitable measure

of the error, Liu and Ponte Castaneda [70] generated the following expression (corresponding to the so-called *energy* version of the second-order theory) for the effective potential of the nonlinear polycrystal [70]:

$$\bar{U}(\Sigma) = \sum_r c^{(r)} \sum_k \left\{ \phi^{k(r)}\left(\hat{\tau}^{k(r)}\right) + \phi'^{k(r)}\left(\bar{\tau}^{k(r)}\right)\left(\bar{\tau}^{k(r)} - \hat{\tau}^{k(r)}\right) \right\} \tag{59}$$

From where the effective response of the homogenized polycrystal can be obtained as $E = \partial \bar{U}(\Sigma)/\partial \Sigma$. The alternate *constitutive equation* version of the second-order theory simply consists in making use of the effective stress–strain rate relations for the linear comparison polycrystal, in which case, e.g. the effective strain is obtained as:

$$E = \sum_r c^{(r)} \sum_k m^{k(r)} \phi'^{k(r)}\left(\bar{\tau}^{k(r)}\right) \tag{60}$$

Both versions of the SO theory give slightly different results, depending on non-linearity and local anisotropic contrast. Such a gap is relatively small compared with the larger variations obtained with the different SC approaches. For variable nonlinearity, the gap between the two second-order model versions exhibits a maximum at an intermediate value of exponent n (between 1 and infinity) and vanishes for these two extreme values. For increasing local anisotropic contrasts, the gap appears to stabilize at sufficient large contrasts [70]. The 'constitutive equation' version is, in principle, less rigorous since it does not derive from a potential function, but has the advantage that can be obtained by simply following the affine algorithm described in the previous sections, using the linearized moduli defined by equations (57) and (58). Therefore, it is the adequate choice to be implemented in the VPSC code.

2.6. *Numerical implementation*

2.6.1. Algorithm. To illustrate the use of this formulation, we describe here the steps required to predict the local and overall viscoplastic response of a polycrystal, for an applied macroscopic velocity gradient, decomposed into the symmetric strain-rate and the skew-symmetric rotation-rate: $U_{i,j} = E_{ij} + \Omega_{ij}$. Mixed boundary conditions (i.e. some components of the macroscopic velocity gradient and some of the macroscopic stress imposed) or fully-imposed macroscopic stress (creep) conditions can be solved as well, with slight variations of the algorithm described below. Starting with an initial Taylor guess, i.e. $\varepsilon^{(r)} = E$ for all grains, we solve the following non-linear equation to get $\sigma^{(r)}$:

$$E = \gamma_o \sum_k m^{k(r)} \left(\frac{m^{k(r)} : \sigma^{(r)}}{\tau_o^{k(r)}} \right)^n \tag{61}$$

and use of an appropriate first-order linearization scheme is made to obtain initial values of $M^{(r)}$ and $\varepsilon^{o(r)}$ for each SR grain (r). Next, initial guesses for the macroscopic moduli $\bar{M}$ and E^o are obtained (usually as simple averages of the local moduli). With them and the applied strain-rate, the initial guess for the macroscopic stress Σ can be obtained (equation (5)), while the Eshelby tensors S and Π can be

calculated using the macroscopic moduli and the ellipsoidal shape of the SR grains via the procedure described in Appendix A. Subsequently, the interaction tensor $\tilde{\mathbf{M}}$ (equation (15)) and the localization tensors $B^{(r)}$ and $b^{(r)}$ (equations (17) and (18)) can be calculated as well. With these tensors, new estimates of $\bar{M}$ and E^o are obtained by solving iteratively the self-consistent equations (21) and (22) (for a unique grain shape) or (23) and (24) (for a distribution of grain shapes). After achieving convergence on the macroscopic moduli (and, consequently, also on the macroscopic stress and the interaction and localization tensors), a new estimation of the average grain stresses can be obtained, using the localization relations (equation (16)). If the recalculated average grain stresses are different (within certain tolerance) from the input values, a new iteration should be started, until reaching convergence. If the chosen linearization scheme is the second-order formulation, an additional loop on the linearized moduli is needed, using the improved estimates of the second-order moments of the stress in the grains, obtained by the methodology described in section 5.1 and Appendices B and C. Otherwise, the iterative procedure is completed and the average shear-rates on the slip (or twinning) of each system (k) in each grain (r) are calculated as:

$$\gamma^{k(r)} = \gamma_o \left(\frac{m^{k(r)} : \sigma^{(r)}}{\tau_o^{k(r)}} \right)^n . \tag{62}$$

These average shear-rates are in turn used to calculate the rotation-rates of the inclusions representing grains and of the lattice associated with each SR grain (a description of how kinematics is dealt with in VPSC can be found in [3]).

It is worth noting that in the case of first-order approximations, although the second-order moments are not needed to readjust iteratively the linearized behaviour of the SR grains, the average field fluctuations associated with the converged values of the effective moduli can be obtained as well, after convergence is reached.

The above numerical scheme can be used either to obtain the anisotropic response of the polycrystal, e.g. probing it along one (or several) strain-paths, by applying strain-rates and obtaining the corresponding stress response, or to predict texture development, by applying viscoplastic deformation in incremental steps. The latter is done by assuming constant rates during a time interval Δt (such that $E\,\Delta t$ corresponds to a macroscopic strain increment in the order of a few percents) and using: (a) the strain-rates and rotation-rates (times Δt) to update the shape and orientation of the SR grains and (b) the shear-rates (times Δt) to update the critical stress of the deformation systems due to strain hardening, after each deformation increment. While any arbitrary hardening law may be implemented, we frequently use an extended Voce law [85], characterized by an evolution of the threshold stress with accumulated shear strain in each grain of the form:

$$\tau^{*k(r)} = \tau_{oo}^k + (\tau_1^k + \theta_1^k \Gamma^{(r)})(1 - \exp(-\Gamma^{(r)} |\theta_o^k / \tau_1^k|)) \tag{63}$$

where $\Gamma^{(r)}$ is the total accumulated shear in the grain; τ_{oo}^k, τ_1^k, θ_o^k and θ_1^k are the initial threshold stress, the initial hardening rate, the asymptotic hardening rate and the back-extrapolated threshold stress, respectively. In addition, we allow for the possibility of 'self' and 'latent' hardening by defining coupling coefficients $h^{kk'}$, which empirically account for the obstacles that new dislocations (or twins)

associated with system k' represent for the propagation of dislocations (or twins) on system k. The increase in the threshold stress is calculated as:

$$\Delta\tau_o^{k(r)} = \frac{\mathrm{d}\tau^{*k(r)}}{\mathrm{d}\Gamma^{(r)}} \sum_{k'} h^{kk'} \gamma^{k'(r)} \Delta t \tag{64}$$

2.6.2. Numerical aspects of the SO implementation. The SO procedure requires iterating over $M_{\mathrm{SO}}^{(r)}$ and $\varepsilon_{\mathrm{SO}}^{o(r)}$ to obtain improved estimations of the linear comparison polycrystal. Each of these trial polycrystals has associated different first- and second-order moments of the stress field in the SR grains. These statistical moments can be used to obtain new values of $\alpha^{k(r)}$ and $e^{k(r)}$, which in turn define a new linear comparison polycrystal, etc. This procedure is terminated when the input and output values of $\alpha^{k(r)}$ and $e^{k(r)}$ coincide within a certain tolerance. This additional iterative procedure is more numerically demanding than the one required by first-order approximations (which in a SO context are also needed, being internal to the linear comparison polycrystal loop). Here, we describe some aspects of the numerical implementation of the external SO loop, which are essential to achieve convergence.

Initial guess for $\alpha^{k(r)}$ and $e^{k(r)}$. The scheme to adjust the values of $\alpha^{k(r)}$ and $e^{k(r)}$ requires the adoption of initial guesses for these magnitudes. The adoption of an 'affine' initial guess usually provides a well-conditioned starting point for the external SO loop. The 'affine' guess reads:

$$\alpha^{k(r)[o]} = n\gamma_o \frac{\left(m^{k(r)} : \sigma^{(r)}\right)^{n-1}}{\left(\tau_o^{k(r)}\right)^n} \tag{65}$$

$$e^{k(r)[o]} = (1-n)\gamma_o \left(\frac{m^{k(r)} : \sigma^{(r)}}{\tau_o^{k(r)}}\right)^n \tag{66}$$

'*Incremental' procedure for low rate-sensitive materials.* If an SO calculation is performed for a low rate-sensitive material (i.e. large n value), the procedure described above for the adjustment $\alpha^{k(r)}$ and $e^{k(r)}$ may fail to converge. In that case, the convergence could be achieved by using incremental steps in the exponent n. Typically, it is necessary to: (a) obtain converged values of $\alpha^{k(r)}$ and $e^{k(r)}$ for the first three values in a sequence of increasing exponents n, (b) use those three initial values of $\alpha^{k(r)}$ and $e^{k(r)}$ to perform a quadratic interpolation for each of these magnitudes, (c) obtain extrapolated estimations of $\alpha^{k(r)}$ and $e^{k(r)}$ to be used as initial guesses for the subsequent exponents in the incremental sequence.

'*Partial' update of $\alpha^{k(r)}$ and $e^{k(r)}$.* Since the values of the second-order moments are strongly dependent on the linear comparison polycrystal (determined from the set of $\alpha^{k(r)}$ and $e^{k(r)}$) and this set is obtained precisely from second-order moments, it is sometimes necessary to adopt a 'partial' update criterion for iterative adjustment of $\alpha^{k(r)}$ and $e^{k(r)}$. For example, if $\alpha^{k(r)[i]}$ and $\alpha^{\mathrm{k}(r)[\mathrm{new}]}$ are, respectively, the current value and the corresponding new estimation of $\alpha^{k(r)}$ obtained by means of equation (54),

a smooth convergence requires the actual updated value be adopted as: $\alpha^{k(r)[i+1]} = (2/3)\alpha^{k(r)[i]} + (1/3)\alpha^{k(r)[\text{new}]}$. Similar 'conservative' update is required for $e^{k(r)}$.

3. Results

3.1. *Model materials*

The advantage of using field fluctuation information in nonlinear homogenization schemes to get improved predictions of the mechanical behaviour and texture development of viscoplastic polycrystals, becomes evident as the heterogeneity (contrast in local properties) increases. The two possible sources of heterogeneity in single-phase viscoplastic aggregates are the nonlinearity of the material's response and the local anisotropy of the constituent single crystals. To study the influence of both sources of heterogeneity, in section 3.2 we show examples of self-consistent calculations on different material systems: (a) fcc aggregates (compatible with, e.g. polycrystalline copper) with fix local anisotropy (given by the, rather mild, range of variation of the Taylor factor of individual grains) and variable rate-sensitivity, and (b) hexagonal polycrystals with four and two soft independent slip systems, and orthorhombic aggregates (compatible with Ti deforming at high temperature, ice and olivine, respectively), with mild nonlinear behaviour and variable local anisotropy, given by the ratio between the threshold resolved shear stresses associated with hard and soft slip modes. In sections 3.3 and 3.4, specific fcc and hcp systems will be considered for the prediction of texture development of rolled low stacking-fault energy (SFE) fcc materials and polycrystalline ice under compression, respectively.

3.2. *Effective behaviour and field heterogeneity*

The prediction of the effective properties of a random fcc polycrystal as the rate-sensitivity of the material decreases is a classical benchmark for the different non-linear SC approaches. Figure 1a (linear scale) and 1b (log scale) show a comparison between average Taylor Factor (TF) versus rate-sensitivity ($1/n$) curves, for a random fcc polycrystal under uniaxial tension. The TF was calculated as Σ_{eq}^{ref}/τ_o, where τ_o is the threshold stress of the $(111)\langle 110\rangle$slip systems and Σ_{eq}^{ref} is the macroscopic equivalent stress corresponding to an applied uniaxial strain-rate with a Von Mises equivalent value $E_{eq}^{ref} = 1$. The curves in figure 1 correspond to the Taylor model, the different first-order SC approximations and the SO procedure. The solid star indicates the rate-insensitive Sachs estimate. The open stars correspond to the 'exact' solution, obtained from ensemble averages of full-field solutions of the governing equations (equilibrium and compatibility), performed on 100 polycrystals with random microstructure, by means of a numerical scheme based on Fast Fourier Transforms (FFT) [86, 87] (for more details on the FFT method and the averaging procedure, see [76]). It can be observed that: (a) the Taylor approach gives the stiffest response, consistent with the upper-bound character of this model; (b) all the SC estimates coincide for $n = 1$, i.e. the linear SC case;

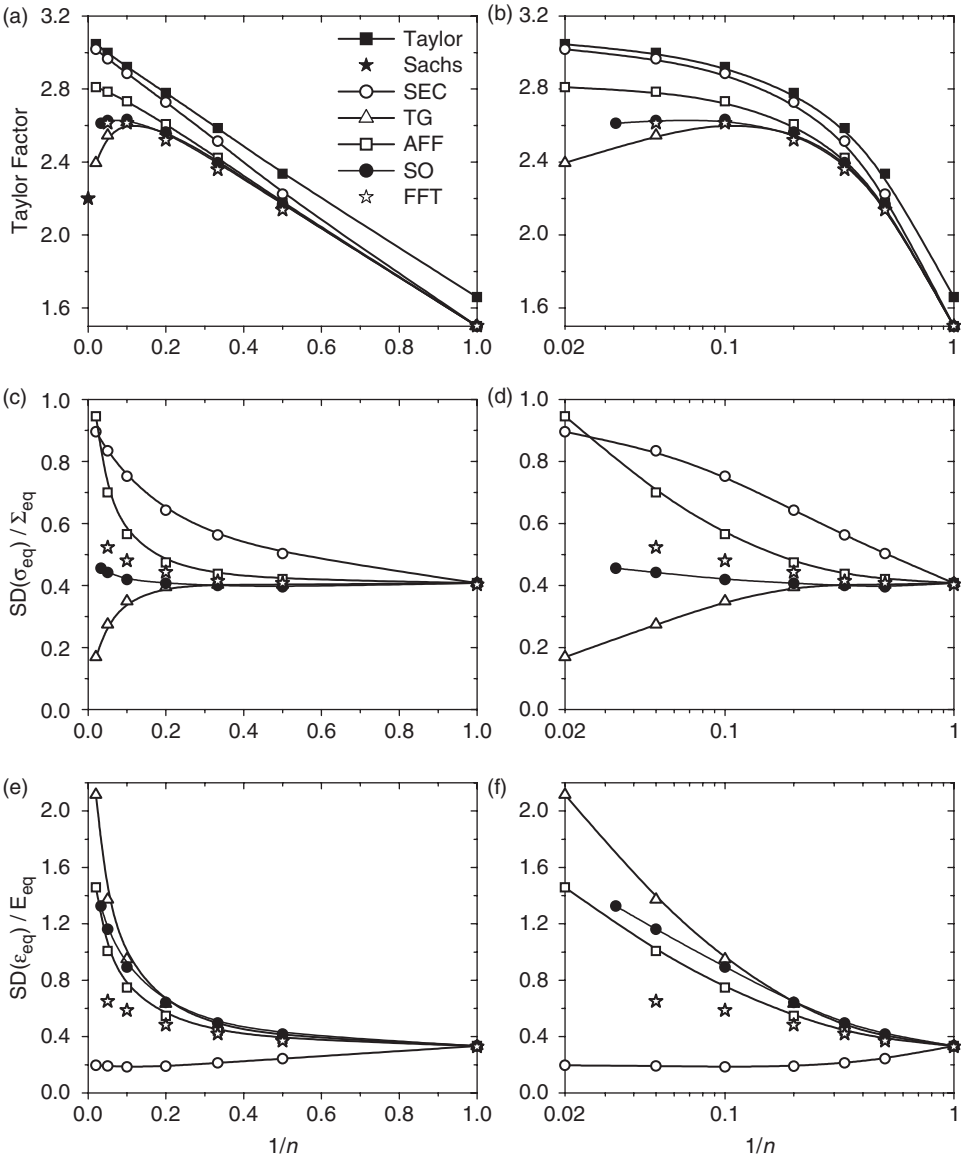

Figure 1. Average Taylor Factor and normalized overall standard deviations versus rate-sensitivity for a random fcc polycrystal under uniaxial tension calculated with the different SC approaches (lines + symbols), and 'exact' values (stars) from ensemble averages of FFT-based solution [76]. Left: linear scale plots; right: log–log plots.

(c) in the rate-insensitive limit, the secant and tangent models tend to the upper- and lower-bounds, respectively, while the affine and second-order approximations remain intermediate with respect to the bounds; (d) except for the tangent model for $n > 10$, the SO procedure gives the lowest TF among the SC approaches.

This softer macroscopic response (i.e. a lower stress is needed to induce a given strain-rate) is a consequence of the softer behaviour at grain level in the linear comparison polycrystal that results when the average field fluctuations are considered for the determination of the linearized behaviour of the SR grains; (e) the best match with the exact solutions (at least for rate-sensitivity exponents up to 20, i.e. the highest value we were able to use in the full-field computations, without loosing accuracy) corresponds to the SO estimates.

Concerning the overall heterogeneity of the mechanical fields, reflected in the standard deviations of the equivalent magnitudes over the whole polycrystal (equations (43) and (44)), the SC predictions (including the SO approximation) are less accurate. Figures 1c and e (linear scale) and figures 1d and f (log scale) show these overall SDs (normalized, for an unbiased comparison, by the corresponding effective magnitudes) as a function of the rate-sensitivity. It can be observed that: (a) at high nonlinearities only the SC models that do not tend to the bounds in the rate-insensitive limit (i.e. AFF and SO) show the expected increases in both stress and strain-rate heterogeneity. In the TG case, the stress heterogeneity decreases as the rate heterogeneity increases, while the SEC approach predicts the opposite trend; (b) both, the AFF and SO approximations overestimate the strain heterogeneity; (c) the SO gives the best match with the full-field predictions for the stress heterogeneity, although it remains below the exact solution. In connection with the SO estimates, the use of the field fluctuations in the linear comparison material to estimate the corresponding fluctuations in the VP polycrystal has recently been shown [88] to be inconsistent. In fact, improved estimates can be generated by taking into account certain correction terms that are associated with the lack of full stationarity of these estimates with respect to the reference stresses. Still, the SC methods would not be expected to yield accurate estimates for the higher-order statistics of the fields, which become increasingly more sensitive to the details of the microstructure as the order increases. For example, the third-order moments, which contain information on the asymmetry of the distributions, are likely to become relatively important in low rate-sensitivity materials [89], since the strain tends to localize in deformation bands inside or across grains.

The next example concerns predictions of the effective behaviour of random aggregates composed by 2000 SR grains with less than five linearly independent soft slip systems. In this case, we analyze the dependence with the local contrast M, given by the ratio between the critical stresses associated with the hard and the soft slip modes. Figure 2 shows the predicted effective stress, relative to the threshold stress of the soft slip systems $\Sigma_{eq}^{ref}/\tau_o^{soft}$ (where Σ_{eq}^{ref} corresponds to an applied uniaxial strain-rate, with a Von Mises equivalent $E_{eq}^{ref} = 1$), as a function the local contrast M, predicted by different homogenization approaches, and by the ensemble averages of exact FFT-based solutions, for the following cases:

(1) A random hcp aggregate with four linearly independent soft slip systems, given by a suitable combination of $\{1010\}\langle 1120\rangle$ prismatic (pr) slip, and $(0001)\langle 1120\rangle$ basal (bas) slip (such that $\tau_o^{soft} = \tau_o^{pr} = \tau_o^{bas}$). The hard slip mode is $\{1011\}\langle 1123\rangle$ pyramidal-$<c+a>$ of the 1st-type (pyr1), and the contrast parameter is, therefore, given by $M = \tau_o^{pyr1}/\tau_o^{pr} = \tau_o^{pyr1}/\tau_o^{bas}$. Assuming a rate-sensitivity exponent $n = 4$ and a c/a ratio of 1.587,

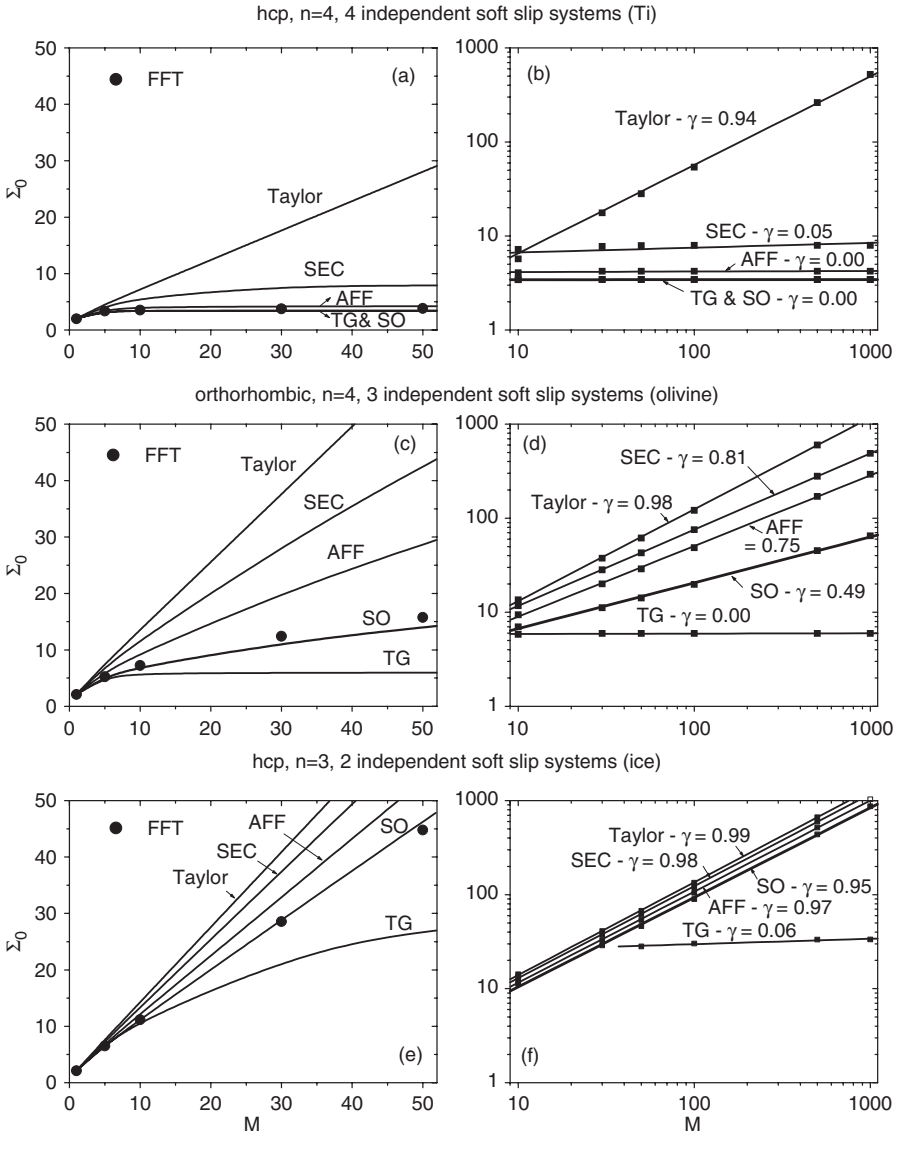

Figure 2. Plots of reference stress versus contrast for random polycrystals with different number of independent soft slip systems obtained with different SC approaches (lines) and from ensemble averages of FFT-based 'exact' solution [76] (symbols). Left column: linear scale plots, up to a contrast of 50. Right column: log–log plots, up to a contrast of 1000. The value of γ correspond to the slope of the logarithmic line.

makes this system compatible with a Ti aggregate deforming at elevated temperatures [90].

(2) A random orthorhombic aggregate, with three linearly independent soft slip systems, given by a suitable combination of (010)[100], (001)[100], (010)[001], (100)[001]. The hard mode, which closes the single crystal yield surface,

is assumed to be $\{111\}\langle 110\rangle$. All the soft systems were assumed to have the same threshold stress τ_o^{soft}, resulting in a contrast parameter $M = \tau_o^{\{111\}}/\tau_o^{soft}$. With a rate-sensitivity exponent $n = 4$ and b/a and c/a ratios of 2.122 and 1.245, respectively, this material system is compatible with an olivine polycrystal, deforming under conditions found in the Earth's upper mantle [44].

(3) A random hcp aggregate with two linearly independent soft systems, corresponding to $\{0001\}\langle 1120\rangle$ basal slip (i.e. $\tau_o^{soft} = \tau_o^{bas}$). The hard slip modes are the $\{1010\}\langle 1120\rangle$ prismatic slip and the $\{1122\}\langle 1123\rangle$ pyramidal-$<c+a>$ of the 2nd-type (pyr2), and the contrast parameter is given by $M = \tau_o^{pr}/\tau_o^{bas} = \tau_o^{pyr2}/\tau_o^{bas}$. Assuming a rate-sensitivity exponent $n = 3$ and a c/a ratio of 1.629, this material system is compatible with an ice polycrystal, deforming under conditions found in glaciers [35].

Figures 2a, c and e show the curves (plotted in linear scale) of reference stress (i.e. $\Sigma_o = \Sigma_{eq}^{ref}/\tau_o^{soft}$, for $E_{eq}^{ref} = 1$) versus contrast M, predicted with the different SC approximations, the Taylor model and the full-field FFT-based solution, for M up to 50. The agreement between the SO estimates and the exact solutions is apparent. Figures 2b, d and f show log–log plots of the effective stress obtained with the different homogenization models, for contrasts up to 1000, with the corresponding regression lines superimposed. It is evident that the results for all models can be described by scaling laws of the form $\Sigma_O \sim M^{\gamma}$ [91]. In every case analyzed ($i = 2$, 3 and 4, where i is the number of linearly independent soft systems), $\gamma \cong 1$ for the Taylor model and $\gamma \cong 0$ for the tangent SC approach (note that the latter exponent also corresponds to the lower-bound Sachs model), while the secant, affine and second-order SC models give different exponents, depending on the value of i. Interestingly, the exponents corresponding to the SO approach follow the relation proposed by Nebozhyn *et al.* [91]: $\gamma \cong (4-i)/2$, in the context of Ponte Castañeda's 1991 variational approach. The asymptotic trend to the lower-bound that the tangent SC approach exhibits when the contrast increases due to the increase of the exponent n (see section 2.4), is also obtained when the heterogeneity increases due to local anisotropy, even for relatively low values of n. This observation sheds light on why the tangent SC approach has been favoured to predict mechanical behaviour of low-symmetry materials (e.g. olivine and related high-pressure silicates [43–46] and ice [35–37]), which have 'open' single crystal yield surfaces with three or less independent deformation systems. In such cases, the tangent SC approach allows accommodation of the local deformation with the available slip systems, without the need of 'artificial' systems to close the single crystal yield surface. While these artificial hard systems make a very small contribution to strain, they have a strong influence on the predicted macroscopic behaviour (effective viscosity) in these low-symmetry systems, unless a saturated behaviour, like the one displayed by the tangent predictions in figure 2, is obtained.

Next, we analyze the field heterogeneity as a function of the contrast parameter M for the above case of the hcp polycrystal with two independent soft slip systems representative of ice. Figures 3a and b show, respectively, the overall stress and strain-rate standard deviations (equations (43) and (44)) that reflect both the intra-phase and the inter-phase field heterogeneities, together with the alternate SD

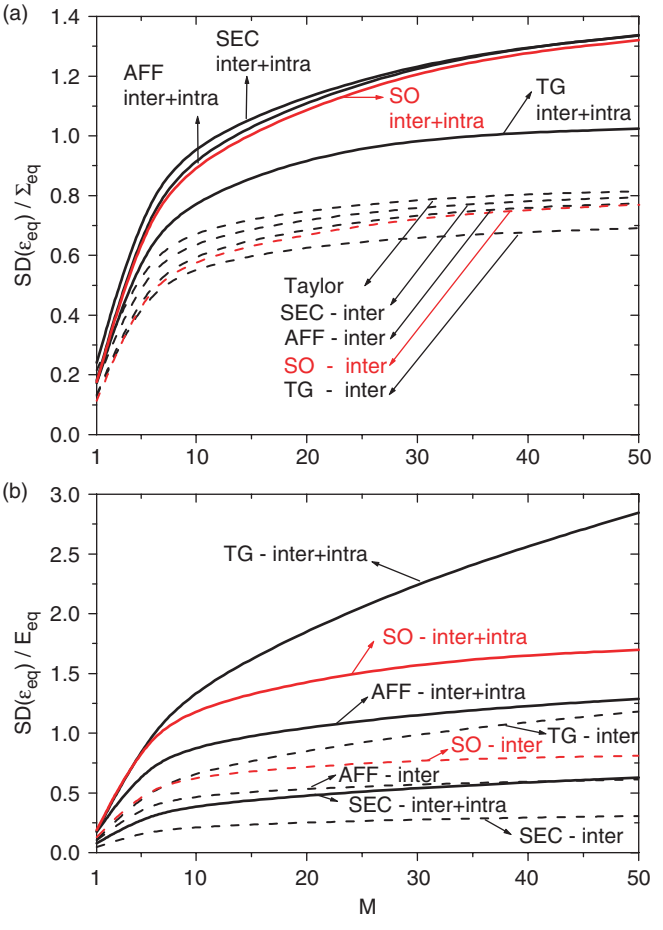

Figure 3. Normalized overall standard deviations of (a) stress and (b) strain-rate versus contrast for the case of a random hcp polycrystal with two independent soft slip systems (ice) obtained with different SC approaches. The *inter* + *intra* and *inter* labels correspond to the SD definitions given by equations (43) and (44), and (47) and (48), respectively.

definitions (equations (47) and (48)) that measure inter-phase fluctuations only, obtained with the different SC approximations (in the Taylor case, only inter-phase SDs can be computed). The following observations can be made: (a) we obtain the expected sequence for the stress heterogeneity indicators (TG < SO < AFF < SEC < Taylor), for the whole range of contrast parameters and for both sets of SDs (note that the reverse sequence is obtained for the strain heterogeneity); (b) the intragranular and intergranular heterogeneities are of the same order for the range of contrast analyzed; (c) within the rather comprehensive interval $1 < M < 5$ the heterogeneities increase linearly with contrast. Concerning the intra-phase strain-rate heterogeneity factor (equation (49)), figure 4 shows its trend to increase as the contrast increases, for the different SC approximations. In the case of the SO approach, the intra-phase strain-rate fluctuations go from

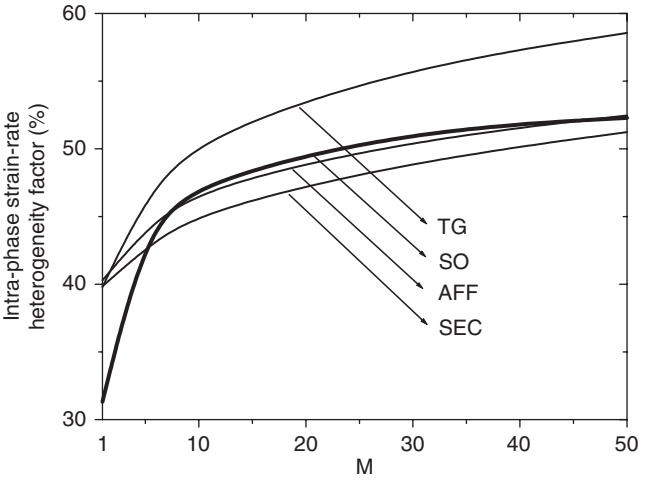

Figure 4. Intra-phase strain rate heterogeneity factor (equation (49)) versus contrast for the case of a random hcp polycrystal with two independent soft slip systems (ice) obtained with different SC approaches.

representing one third of the total heterogeneity for $M = 1$ to more than a half, for $M = 50$. This is an indication that, as the local anisotropy increases, the behaviour of a grain is more sensitive to its particular environment and, concomitantly, the strain-rate field inside the grains is more heterogeneous.

3.3. *Texture evolution of fcc polycrystals under plane-strain*

Predicting the brass-type texture in cold-rolled low-SFE fcc materials and, more importantly, understanding the microstructural reasons leading to the formation of this texture is a classical problem in the texture community (for a comprehensive review, see [92]). Even if the initial material does not usually exhibit a particularly high local anisotropy (e.g. a recrystallized aggregate), it is now well established that the microstructural evolution in low-SFE fcc materials is characterized by the appearance of very thin mechanical twins in a significant fraction of grains. The twins induce a strong plastic anisotropy in those grains. As a consequence, we expect that the different SC approaches should give significantly different predictions of texture evolution in low SFE fcc, when this induced anisotropy is accounted for.

Leffers and Juul Jensen [93] have characterized the microstructural evolution of cold-rolled brass (15% zinc) by these salient features: (a) mechanical twins appear at early stages of deformation, in about 40% of the (initially randomly oriented) grains, (b) the twins are very thin and, therefore, make a minor volumetric contribution to texture (as opposed to the strong contribution of twinning to texture evolution in, e.g., hcp metals), (c) twin 'bundles' usually lie parallel to a particular {111} plane, i.e. the twin plane, (d) twins act as effective barriers to dislocations gliding on {111} planes different from the twin plane, therefore 'coplanar' single slip

(i.e. glide on one favourably-oriented system), with the slip plane coincident with the twin plane of the predominant twins, is strongly favoured in grains with twins. Based on this observed trend towards a single slip pattern in a large fraction of grains, in the early days of texture development simulation a modified Sachs model was proposed [94] to explain the formation of the brass-type texture. Later, the tangent SC model was utilized, using a high n exponent to force a similar close-to-lower-bound behaviour [14]. In what follows, we revisit the brass-type texture prediction, using the different SC approaches described in previous sections.

To accurately account for the local anisotropy evolution associated with mechanical twinning, we have proceeded as follows (see also [95]). The set of 1000 randomly generated orientations representing the initial low-SFE fcc polycrystal was preprocessed under the assumption that $\{111\}\langle 110\rangle$ slip and $\{111\}\langle 112\rangle$ twinning were the active deformation modes, with the same threshold stress. Applying a state of plane-strain compression, we identified for each orientation the first and second most active deformation systems. In this way, 418 of the 1000 grains were identified, in which the geometrically favoured deformation systems were one slip system and one twinning system sharing the same slip/twinning plane (note the good agreement with the aforementioned observations [93] of about 40% of grains with twins in cold-rolled 15%-zinc brass). These grains were then 'marked' to have a strong non-coplanar latent hardening (NCLH), such that $h^{kk'}=1$ for systems k and k' having the same slip plane, and $h^{kk'}=5$ for k and k' gliding on different planes (see equation (64)). The remaining 582 grains were assigned an isotropic hardening: $h^{kk'}=1.5$ for all k and k'. The adopted values of the other hardening parameters were: $\tau_{oo}^{k}=\tau_{1}^{k}=16\,\mathrm{MPa}$, $\theta_{o}^{k}=320\,\mathrm{MPa}$ and $\theta_{1}^{k}=16\,\mathrm{MPa}$, $(k=1,12)$ (see equation (63)). In this way, the sets of 'marked' and 'non-marked' grains represent a 'two-phase' material, where both sets have initially the same local mechanical response, but which, due to different hardening laws associated with the likely presence of twins in the 'marked' grains, evolve differently, with coplanar slip strongly favoured in the 'marked' grains. Only the effect of twinning on the hardening of non-coplanar slip modes was taken into account in these simulations and reorientation due to twinning was not considered, since experimental evidence indicates little volumetric effect of twinning on texture [92, 93].

Figure 5 shows the results of rolling simulations (plane-strain compression) up to a strain of two in the rolling direction (86% thickness reduction), carried out with different SC approaches, rate sensitivity exponents and microstructure evolution assumptions. For each case, the $\{111\}$ and $\{100\}$ pole figures are shown, together with the evolution of the ideal rolling components and the average number of active systems (AVACS) per grain. A given orientation is assigned to the $\{112\}\langle 111\rangle$ copper (Cu), $\{110\}\langle 112\rangle$ brass (B), $\{123\}\langle 634\rangle$ S, $\{110\}\langle 001\rangle$ Goss (G), or $\{100\}\langle 001\rangle$ cube (C) component if it is within a misorientation smaller than 15° from the component (figure 6 shows the $\{111\}$ and $\{100\}$ poles corresponding to those ideal components). The 'other' component corresponds to orientations not belonging to any of the above. The AVACS in a grain was defined by the number of slip systems having shear-rates higher than 5% of the shear-rate of the most active system. The first column corresponds to a tangent SC simulation, without NCLH, and $n=40$. This close-to-lower-bound calculation (see figure 1 and note the low AVACS values in figure 5) shows the development of a strong brass component, at the expense of all

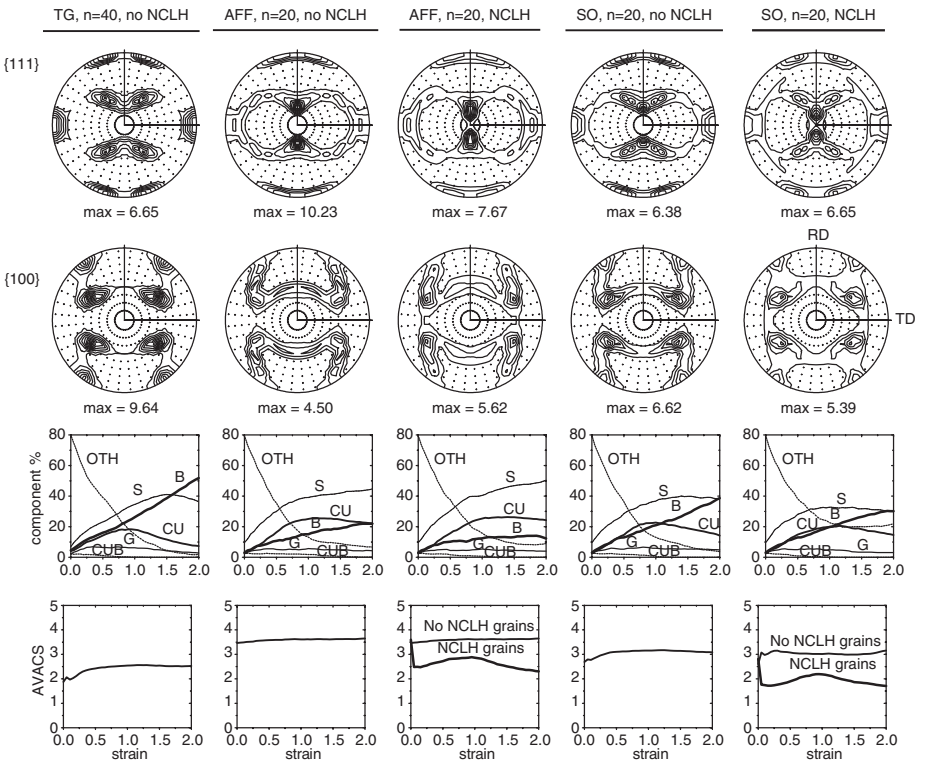

Figure 5. Simulated rolling textures of an fcc polycrystal obtained with various SC approaches and under different assumptions of microstructure evolution. Rows: 1st and 2nd are final {111} and {100} pole figures for a strain of two in the rolling direction (level lines correspond to multiples of random distribution, mrd); 3rd is evolution of the volume fraction of ideal fcc rolling components and the 4th row is average number of active systems per grain (AVACS). Columns: 1st is tangent SC approach ($n=40$) isotropic hardening; 2nd and 3rd rows are affine SC results ($n=20$) isotropic and non-coplanar latent hardening, respectively; 4th and 5th are second-order simulations ($n=20$) isotropic and non-coplanar latent hardening, respectively.

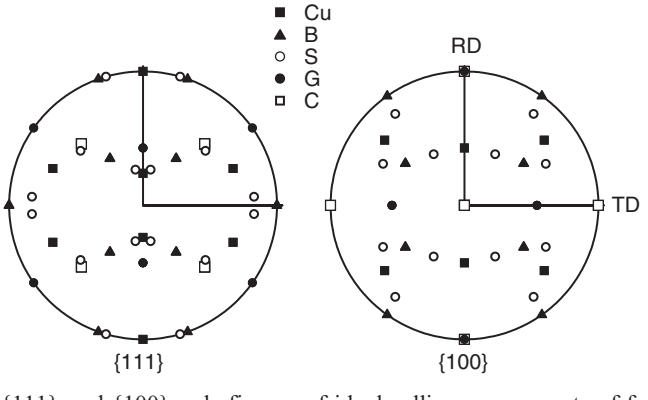

Figure 6. {111} and {100} pole figures of ideal rolling components of fcc materials.

the other ideal components. This predominance of the brass *component* results in a rolling texture quite different from the brass-type *texture*, which is characterized by a balanced content of B and S, with minor fractions of G and Cu [96], as well as by a non-negligible contribution of grains with {111} planes parallel to the rolling plane (not counted as part of any of the ideal components) [92]. The second and third columns show the results of the affine SC formulation for $n = 20$, without and with NCLH in 'marked' grains, respectively. The resulting texture for the no NCLH case is a copper-type texture, i.e. high proportion of S-component, followed by a balanced contribution of Cu and B [96]. The incorporation of twinning-induced hardening mechanisms via the NCLH in 'marked' grains gives a component of orientations having their {111} poles near the normal direction, but at the expense of reducing the B-component, resulting in a departure from both the copper-type and the brass-type textures.

The forth and fifth columns show the SO results. Without NCLH, the resulting texture has a balanced S- and B-content, and minor Cu- and G-contents, but the {111}//ND component is missing. When the selective NCLH is assumed, the right proportions of S, B, Cu and G are also obtained, together with a component of grains with their {111} poles near (but not exactly at) ND (note that these orientations are responsible for the relative increase of the 'other' component at the expense of S and B). Interestingly, the latter orientations overwhelmingly correspond to grains with NCLH. The slip activity of these grains tend to concentrate on one particular {111} plane very rapidly (see corresponding AVACS curve), leading to a local strain state closer to simple shear, rather than the macroscopically imposed plane-strain compression. The combined effect of morphologic evolution (the grains become flat) and the aforementioned local simple shear state in NCLH grains, tends to align the crystallographic shear plane (i.e. a {111}-plane) within a few degrees from the macroscopic shear plane (i.e. the rolling plane), giving two maxima near ND, instead of the observed {111} at ND. This deviation from the actual {111}//ND condition may be due to the fact that, although the intragranular fluctuations are taken into account in an SO calculation, the reorientation of the SR grains is still carried out using the average values of plastic rotations (see equation (62) and discussion thereafter). The use of the NCLH strategy combined with models that take into account the intragranular heterogeneity in the determination of local rotations should give the elusive {111}//ND component of the brass-type texture [95].

3.4. *Texture evolution of ice aggregates under compression*

In ice, almost all the deformation in the single crystals is carried by basal dislocations. Since basal slip provides only two independent slip systems, the prediction of texture development of polycrystalline ice is a challenging problem that allows us to discriminate among the different SC approaches. Moreover, an understanding of the deformation mechanisms and the microstructural evolution of ice deforming in compression is relevant in glaciology, since compression (together with shear) is one of the main deformation modes of glaciers. In what follows, we will use the *basal texture factor* along the axial direction to characterize the evolving texture of ice in compression. The basal texture factor is defined as

the weighted average of the projections of the c-axes along the axial direction, i.e. $\langle \cos^2 \alpha^{(r)} \rangle$ (where $\alpha^{(r)}$ is the angle between the basal pole of SR grain (r) and the axial compression direction).

On the one hand, the stiff Taylor and SC secant models are not suitable to simulate plastic deformation of polycrystalline ice because the strong constraints that these models impose upon strain are incompatible with the shortage of independent slip systems in ice. On the other hand, the compression textures of ice typically exhibit a strong basal pole component aligned with the axial direction [35]. The formation of this component is related to the crystallographic plastic rotations associated with basal slip. However, as the basal poles become aligned with the axial direction, the basal systems become unfavourably oriented to accommodate deformation. Therefore, at large strains, even a 'soft' first-order approximation like the tangent SC fails in reproducing the observed texture with only basal slip activity [35]. Up to now, the Sachs model (which completely disregards strain compatibility) has been the only approach able to give a reasonable effective behaviour with predominant basal slip at large strains, when the basal texture along the compressive direction becomes very strong.

Figure 7 shows the compression texture evolution (in terms of the basal texture factor), the effective stress, the relative basal activity and the average number of active slip systems (AVACS) per grain for the case of an initially random ice polycrystal. Results were obtained using the TG, AFF and SO approaches, under the assumption of $n = 3$ and $\tau_o^{pr} = 20 \times \tau_o^{bas}$ and $\tau_o^{pyr2} = 200 \times \tau_o^{bas}$, as reported in [35], with no strain-hardening, up to a compressive strain of 1.5.

As expected, all models predict a prevalence of basal slip, with a consequent increase of the basal texture factor along the axial direction and a progressive geometric hardening. While the alignment of basal poles along the compression direction predicted by all three models is similar, they differ in other indicators. At around 0.8 strain, the tangent predictions show a sudden drop in the basal activity, together with a rapid increase in the effective stress and in the number of active deformation systems, which indicates that the strain accommodation starts requiring the activation of the 200 times harder pyramidal systems. In other words, under the tangent SC approach, the basal slip by itself is not enough to accommodate the compressive deformation when the basal poles become strongly aligned with the compression direction.

The SO and AFF models, on the other hand, do a better job at accommodating large strain mostly with basal slip. The SO results, however, are superior to the AFF results in this respect. This superior performance of the second-order SC approximation can be explained in terms of its intrinsic adaptability to microstructural changes. Figure 8 shows the evolution (as predicted with the SO formulation) of the normalized standard deviations of the equivalent stress and strain-rate over the whole polycrystal, defined by equations (43) and (44). Note that the above magnitudes are indicators not only of intergranular but also of intragranular heterogeneity (as a matter of fact, these average scalar magnitudes reflect the collective contribution of every component of the fluctuation tensors in each SR grain). Evidently, as the basal texture concentrates along the axial direction, the stress becomes more uniform and the strain-rate becomes more heterogeneous. This trend towards a uniform stress state obviously indicates a trend towards the

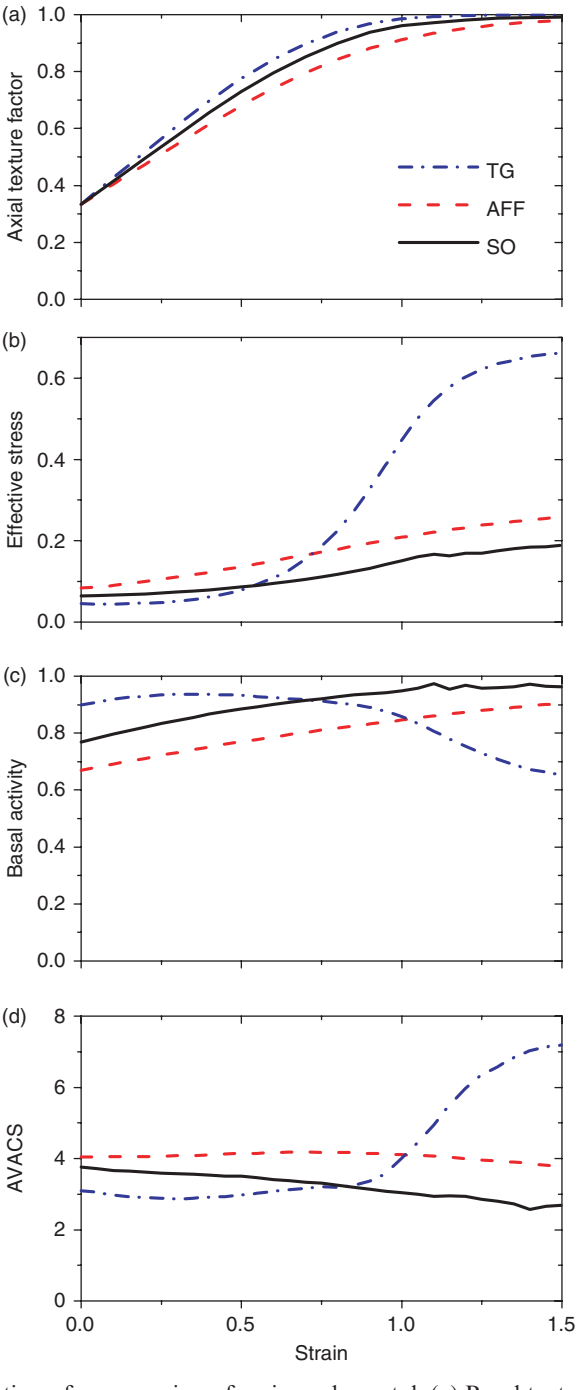

Figure 7. Simulation of compression of an ice polycrystal. (a) Basal texture factor along the compression direction, (b) Effective stress, (c) Relative basal activity and (d) The average number of active slip systems per grain, as predicted with the tangent, affine and second-order SC approaches.

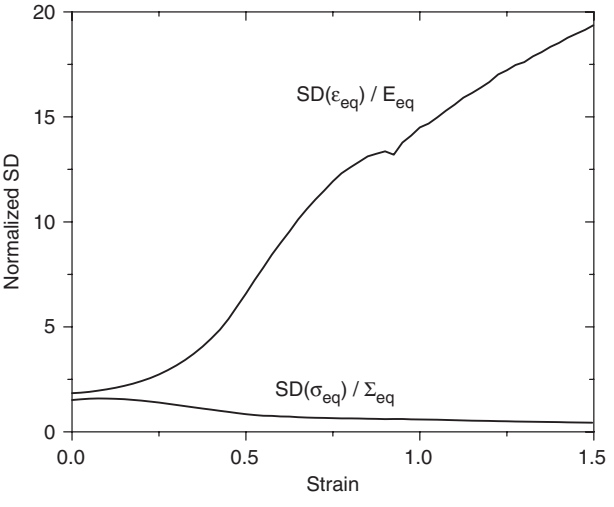

Figure 8. Evolution of the normalized overall standard deviations of the equivalent stress and strain rate, as predicted with the SO formulation, for the case of compression of ice.

Sachs condition. Therefore, given that the aforementioned local fluctuation information is contained in the SO linearization, the SO results approach the lower-bound as deformation proceeds, allowing a substantial accommodation of deformation by basal slip at those large strains.

4. Conclusions

This paper provides a comprehensive description and a detailed comparative discussion of the different self-consistent formalisms for viscoplastic polycrystals. We also present the numerical implementation of the different SC approaches in the VPSC code, together with a critical comparison of results obtained with different linearization strategies. Specifically, predictions of mechanical response and texture development obtained with the different SC formulations were compared with full-field simulations and also discussed in light of available experimental evidence.

Comparison of the effective behaviour of model material systems predicted by different SC approaches shows that the second-order SC predictions are in better agreement with the 'exact' full-field solutions. The latter is especially true in the cases of highly heterogeneous materials (due to a strong nonlinearity or local anisotropy), a case in which the gap between the Taylor and the Sachs bounds is large. In particular, we show that the scaling law, proposed in the context of an earlier variational formulation for systems with less than five independent soft slip systems [91], also holds for the second-order approach and, more importantly, agrees very well with the full-field solutions.

Concerning the predictions of field heterogeneity, we distinguish between inter-granular and intra-granular heterogeneity, and show that they are of the

same order and give a measure of the relative values of these two indicators. In general, the predictions of overall field heterogeneity are less accurate for every SC linearization scheme tested in this work, compared with the full-field results. This is because higher-order statistics are expected to be increasingly sensitive to the specific microstructure, especially when significant nonlinearities are involved.

With regard to the application of the second-order approximation to texture development, we have studied two cases, characterized by a strong local anisotropy, due either to inherent contrast of plastic properties at single crystal level (ice) or to microstructure evolution (twins in low-SFE fcc). In both cases, some variant of the oversimplified Sachs model had been used in the past to explain the texture evolution of these materials. Here, we have shown the flexibility of the second-order formulation to handle these highly anisotropic problems.

Finally, it is worth mentioning that, although the information on intragranular field fluctuations is accounted for in the second-order procedure, in the present implementation, the reorientation and strain-hardening of the SR grains is still carried out using the average values of the shear-rates in the grains only. If the average fluctuations of the shear-rates for each slip system of each SR grain could be obtained, improved schemes for updating grain orientations and critical stresses, which take into account the effect of intragranular heterogeneities, could be implemented. Such an improved treatment of strain-hardening was recently performed in the restricted context of linearly viscous 2-D polycrystals [97]. The extension to more general problems of this kind of updating schemes, containing intragranular heterogeneity information, is currently under investigation.

Acknowledgments

The authors wish to thank Dr Torben Leffers (RISØ National Laboratory, Denmark) for his insights on the brass-type texture and for making his review paper on this subject available prior to publication, Dr Martin Idiart (University of Pennsylvania, USA) for his valuable comments on algorithmic aspects of field fluctuation calculation and Dr Olivier Castelnau (CNRS-Université Paris XIII, France) for discussions on the viscoplastic deformation of polycrystalline geomaterials. The work of PPC was supported by DOE grant DE-FG02-04ER46110.

Appendix A: Green function solution of the viscoplastic inclusion problem

From equation (10), the fictitious volumetric force associated with the heterogeneity is:

$$f_i(\bar{\mathbf{x}}) = -\bar{L}_{ijkl}\varepsilon^*_{kl,j}(\bar{\mathbf{x}}) = \sigma^*_{ij,j}(\bar{\mathbf{x}}) \tag{A1}$$

The field $\sigma^*_{ij}(\bar{\mathbf{x}}) = -\bar{L}_{ijkl}\varepsilon^*_{kl}(\bar{\mathbf{x}})$ is an eigen-stress field. System (9) consists of four differential equations with four unknowns: three are the components of velocity

deviation vector $\tilde{u}_i(\bar{\mathbf{x}})$, and one is the mean stress deviation $\tilde{\sigma}^m(\bar{\mathbf{x}})$. Such system of N linear differential equations with N unknown functions and an inhomogeneity term can be solved using the Green function method, as explained in what follows. Let us call $G_{km}(\bar{\mathbf{x}})$ and $H_m(\bar{\mathbf{x}})$ the Green functions associated with $\tilde{u}_i(\bar{\mathbf{x}})$ and $\tilde{\sigma}^m(\bar{\mathbf{x}})$, which solve the auxiliary problem of a unitary volumetric force, with a single non-vanishing m-component, and applied at $\bar{\mathbf{x}} = 0$:

$$\begin{vmatrix} \bar{L}i_{jkl}G_{km,lj}(\bar{\mathbf{x}}) + H_{m,i}(\bar{\mathbf{x}}) + \delta_{im}\delta(\bar{\mathbf{x}}) = 0 \\ G_{km,k}(\bar{\mathbf{x}}) = 0 \end{vmatrix} \tag{A2}$$

Once the solution of (A2) is obtained, the solution for the velocity field is given by the convolution integrals:

$$\tilde{u}_k(\bar{\mathbf{x}}) = \int_{R^3} G_{ki}(\bar{\mathbf{x}} - \bar{\mathbf{x}}')f_i(\bar{\mathbf{x}}')\mathrm{d}\bar{\mathbf{x}}' \tag{A3}$$

System (A2) can be solved using the Fourier transform method. Expressing the Green functions in terms of their inverse Fourier transforms, the differential system (A2) transforms into an algebraic system:

$$\begin{vmatrix} \alpha_j\alpha_l\bar{L}_{ijkl}k^2\hat{G}_{km}(\bar{k}) + \alpha_i ik\hat{H}_m(\bar{k}) = \delta_{im} \\ \alpha_k k^2\hat{G}_{km}(\bar{k}) = 0 \end{vmatrix} \tag{A4}$$

where k and $\bar{\alpha}$ are the modulus and the unit vector associated with a point of Fourier space $\bar{k} = k\bar{\alpha}$, respectively. Calling $A^d_{ik} = \alpha_j\alpha_l\bar{L}_{ijkl}$, system (A4) can be expressed as a matrix product $A \times B = C$, where A, B and C are matrices given by:

$$\begin{array}{c|ccc} & k^2\hat{G}_{11} & k^2\hat{G}_{12} & k^2\hat{G}_{13} \\ & k^2\hat{G}_{21} & k^2\hat{G}_{22} & k^2\hat{G}_{23} \\ & k^2\hat{G}_{31} & k^2\hat{G}_{32} & k^2\hat{G}_{33} \\ & ik\hat{H}_1 & ik\hat{H}_2 & ik\hat{H}_3 \end{array} = B$$

$$A = \begin{array}{cccc|ccc} A^d_{11} & A^d_{12} & A^d_{13} & \alpha_1 & 1 & 0 & 0 \\ A^d_{21} & A^d_{22} & A^d_{23} & \alpha_2 & 0 & 1 & 0 \\ A^d_{31} & A^d_{32} & A^d_{33} & \alpha_3 & 0 & 0 & 1 \\ \alpha_1 & \alpha_2 & \alpha_3 & 0 & 0 & 0 & 0 \end{array} = C \tag{A5}$$

The 4×4 matrix A is real and symmetric. As a consequence, its inverse will also be real and symmetric. Using the explicit form of matrix C, we can write the solution of (A5) as:

$$B = A^{-1} \times C = \begin{bmatrix} A^{-1}_{11} & A^{-1}_{12} & A^{-1}_{13} \\ A^{-1}_{21} & A^{-1}_{22} & A^{-1}_{23} \\ A^{-1}_{31} & A^{-1}_{32} & A^{-1}_{33} \\ A^{-1}_{41} & A^{-1}_{42} & A^{-1}_{43} \end{bmatrix} \tag{A6}$$

Finally, comparing (A5) and (A6):

$$k^2\hat{G}_{ij} = A_{ij}^{-1} \ (i,j = 1,3) \tag{A7}$$

Since the components of A are real functions of α_i, so are the components of A^{-1} and so are those of $k^2\hat{G}_{ij}$. This property leads to real integrals in the derivation that follows.

Knowing the Green tensor expression in Fourier space, we can write the solution of our eigen-strain-rate problem using the convolution integral. Taking partial derivatives to equation (A3) we obtain:

$$\tilde{u}_{k,l}(\bar{\mathbf{x}}) = \int_{R^3} G_{ki,l}(\bar{\mathbf{x}} - \bar{\mathbf{x}}')f_i(\bar{\mathbf{x}}')\mathrm{d}\bar{\mathbf{x}}' \tag{A8}$$

Replacing (A1) in (A8), recalling that $\partial G_{ij}(\bar{\mathbf{x}} - \bar{\mathbf{x}}')/\partial\bar{\mathbf{x}} = -\partial G_{ij}(\bar{\mathbf{x}} - \bar{\mathbf{x}}')/\partial\bar{\mathbf{x}}'$, integrating by parts, and using the divergence theorem [78], we obtain:

$$\tilde{u}_{k,l}(\bar{\mathbf{x}}) = \int_{R^3} G_{ki,jl}(\bar{\mathbf{x}} - \bar{\mathbf{x}}')\sigma^*_{ij}(\bar{\mathbf{x}}')\mathrm{d}\bar{\mathbf{x}}' \tag{A9}$$

Equation (A9) provides an exact implicit solution to the problem. Such solution requires knowing the local dependence of the eigen-stress tensor. However, we know from the elastic Eshelby inclusion formalism that if the eigen-strain is uniform over an ellipsoidal domain where the stiffness tensor is uniform, then the stress and the strain are constant over the domain of the inclusion (r). The latter suggests assuming an eigen-stress of constant value (*a priori* unknown) within the volume Ω of an ellipsoidal inclusion and zero outside. This allows us to average the local field (A11) over the domain Ω and obtain an average strain-rate inside the inclusion of the form:

$$\tilde{u}^{(r)}_{k,l} = \left(-\frac{1}{\Omega}\int_\Omega\int_\Omega G_{ki,jl}(\bar{\mathbf{x}} - \bar{\mathbf{x}}')\mathrm{d}\bar{\mathbf{x}}\,\mathrm{d}\bar{\mathbf{x}}'\right)\bar{L}_{ijmn}\varepsilon^{*(r)}_{mn} \tag{A10}$$

where $\tilde{u}^{(r)}_{k,l}$ and $\varepsilon^{*(r)}_{mn}$ have to be interpreted as average quantities inside the inclusion. Expressing the Green tensor in terms of the inverse Fourier transform and taking derivatives we obtain:

$$\begin{aligned}\tilde{u}^{(r)}_{k,l} &= \left(\frac{1}{8\pi^3\Omega}\int_\Omega\int_\Omega\int_{R^3}\alpha_j\alpha_l\left(k^2\hat{G}_{ki}(\bar{k})\right)\exp\left[-i\bar{k}(\bar{\mathbf{x}} - \bar{\mathbf{x}}')\right]\mathrm{d}\bar{k}\,\mathrm{d}\bar{\mathbf{x}}\,\mathrm{d}\bar{\mathbf{x}}'\right)\bar{L}_{ijmn}\varepsilon^{*(r)}_{mn} \\ &= T_{klij}\bar{L}_{ijmn}\varepsilon^{*(r)}_{mn}\end{aligned} \tag{A11}$$

Writing $\mathrm{d}\bar{k}$ in spherical coordinates: $\mathrm{d}\bar{k} = k^2\sin\theta\,\mathrm{d}k\,\mathrm{d}\theta\,\mathrm{d}\varphi$ and using relation (A7), the Green interaction tensor T_{klij} can be expressed as:

$$T_{klij} = \frac{1}{8\pi^3\Omega}\int_0^{2\pi}\int_0^{\pi}\alpha_j\,\alpha_l\,A^{-1}_{ki}(\bar{\alpha})\ \Lambda(\bar{\alpha})\ \sin\theta\,\mathrm{d}\theta\,\mathrm{d}\varphi \tag{A12}$$

where θ and φ are the spherical coordinates of the Fourier unit vector $\bar{\alpha}$ and:

$$\Lambda(\bar{\alpha}) = \int_0^\infty\left(\int_\Omega\int_\Omega\exp\left[-i\bar{k}(\bar{\mathbf{x}} - \bar{\mathbf{x}}')\right]\mathrm{d}\bar{\mathbf{x}}\,\mathrm{d}\bar{\mathbf{x}}'\right)k^2\mathrm{d}k \tag{A13}$$

Integrating (A13) inside an ellipsoidal grain of radii(a, b, c) [98] and replacing in (A12) gives:

$$T_{klij} = \frac{abc}{4\pi}\int_0^{2\pi}\int_0^{\pi}\frac{\alpha_j\alpha_l A_{ki}^{-1}(\bar{\alpha})}{[\rho(\bar{\alpha})]^3}\sin\theta\,\mathrm{d}\theta\,\mathrm{d}\varphi \tag{A14}$$

where $\rho(\bar{\alpha}) = \left[(a\alpha_1)^2 + (b\alpha_2)^2 + (c\alpha_3)^2\right]^{1/2}$. The symmetric and skew-symmetric Eshelby tensors are defined as:

$$S_{ijkl} = \frac{1}{4}\left(T_{ijmn} + T_{jimn} + Ti_{jnm} + T_{jinm}\right)\bar{L}_{mnkl} \tag{A15}$$

$$\Pi_{ijkl} = \frac{1}{4}\left(T_{ijmn} - T_{jimn} + T_{ijnm} - T_{jinm}\right)\bar{L}_{mnkl} \tag{A16}$$

Taking symmetric and skew-symmetric components to (A11) and using (A15) and (A16), we obtain the average strain-rate and rotation-rate deviations in the ellipsoidal domain:

$$\tilde{\varepsilon}^{(r)} = S : \varepsilon^{*(r)} \tag{A17}$$

$$\tilde{\omega}^{(r)} = \Pi : \varepsilon^{*(r)} = \Pi : S^{-1} : \tilde{\varepsilon}^{(r)} \tag{A18}$$

Appendix B: Calculation of effective moduli derivatives

Calculation of $\partial B_{kj}^{(s)}/\partial M_{uv}^{(r)}$: From equation (17), we have (in matrix notation, all indices running from 1 to 5, except the grain indices (r) and (s)):

$$\frac{\partial B_{kj}^{(s)}}{\partial M_{uv}^{(r)}} = -\left(M^{(s)} + \tilde{M}\right)_{ku}^{-1}\delta_{rs}B_{vj}^{(s)} + \left(M^{(s)} + \tilde{M}\right)^{-1}\cdot\left[\frac{\partial\tilde{M}}{\partial M_{uv}^{(r)}}\cdot\left(I - B^{(s)}\right) + \frac{\partial\tilde{M}}{\partial M_{uv}^{(r)}}\right]. \tag{B1}$$

So as not to clutter the notation, the first and second term on the right are written in explicit and implicit index notation, respectively. In the second term the indices (uv) (i.e. the component of the local compliance with respect to which the derivatives are calculated) appear only to indicate such derivative, while in the first term they appear mixed with the indices that contract. In what follows, we will use this mix of explicit indices and implicit notation, when necessary for the sake of clarity.

Deriving expression (15) we obtain:

$$\frac{\partial\tilde{M}_{ij}}{\partial M_{uv}^{(r)}} = (I - S)_{ik}^{-1}\frac{\partial S_{kl}}{\partial M_{uv}^{(r)}}\psi_{lj} + F_{ip}^{S}\frac{\partial\bar{M}_{pj}}{\partial M_{uv}^{(r)}} \tag{B2}$$

where $F^S = (I - S)^{-1}S$ and $\psi = F^S\cdot\tilde{M} + \tilde{M}$. Using the chain rule to express the first derivative on the right, we can write:

$$\frac{\partial\tilde{M}_{ij}}{\partial M_{uv}^{(r)}} = (I - S)_{ik}^{-1}\frac{\partial S_{kl}}{\partial\bar{M}_{pq}}\frac{\partial\bar{M}_{pq}}{\partial M_{uv}^{(r)}}\psi_{lj} + F_{ip}^{S}\frac{\partial\bar{M}_{pj}}{\partial M_{uv}^{(r)}} = \theta_{ijpq}\frac{\partial\bar{M}_{pq}}{\partial M_{uv}^{(r)}} \tag{B3}$$

where

$$\theta_{ijpq} = (I - S)^{-1}_{ik} \frac{\partial S_{kl}}{\partial \bar{M}_{pq}} \psi_{lj} + F^{S}_{ip} \delta_{jq} \tag{B4}$$

The algorithm for the calculation of $\partial S/\partial \bar{M}$ is given in Appendix C. Replacing (B3) in (B1) and after some manipulation we obtain:

$$\frac{\partial B^{(s)}_{kj}}{\partial M^{(r)}_{uv}} = -\chi^{(s)}_{ku} \delta_{rs} B^{(s)}_{vj} + \chi^{(s)} \cdot \alpha^{(s)} : \frac{\partial \bar{M}}{\partial M^{(r)}_{uv}} \tag{B5}$$

where:

$$\chi^{(s)} = \left(M^{(s)} + \tilde{M} \right)^{-1} \tag{B6}$$

$$\alpha^{(s)}_{ijkl} = \theta_{imkl} \left(I - B^{(s)} \right)_{mj} + \delta_{ik} \delta_{jl} \tag{B7}$$

Calculation of $\partial \bar{M}_{ij}/\partial M^{(r)}_{uv}$: Deriving equation (32):

$$\frac{\partial \bar{M}_{ij}}{\partial M^{(r)}_{uv}} = \sum_s c^{(s)} \delta_{iu} \delta_{kv} \delta_{rs} B^{(s)}_{kj} + \sum_s c^{(s)} M^{(s)}_{ik} \frac{\partial B^{(s)}_{kj}}{\partial M^{(r)}_{uv}} \tag{B8}$$

Using (B5) and calling $\beta^{(s)} = M^{(s)} \cdot \chi^{(s)}$ we get:

$$\frac{\partial \bar{M}_{ij}}{\partial M^{(r)}_{uv}} = c^{(r)} \delta_{iu} B^{(r)}_{vj} - c^{(r)} \beta^{(r)}_{iu} B^{(r)}_{vj} + \left(\sum_s c^{(s)} \beta^{(s)} \cdot \alpha^{(s)} \right) : \frac{\partial \bar{M}}{\partial M^{(r)}_{uv}} \tag{B9}$$

From where:

$$\Omega_{ijkl} \frac{\partial \bar{M}_{kl}}{\partial M^{(r)}_{uv}} = \pi^{(r,uv)}_{ij} \tag{B10}$$

with:

$$\pi^{(r,uv)}_{ij} = c^{(r)} \left(\delta_{iu} - \beta^{(r)}_{iu} \right) B^{(r)}_{vj} \tag{B11}$$

$$\Omega_{ijkl} = \delta_{ik} \delta_{jl} - \sum_s c^{(s)} \beta^{(s)} \cdot \alpha^{(s)} \tag{B12}$$

Calculation of $\partial E^{o}_{j}/\partial M^{(r)}_{uv}$: Deriving equation (33):

$$\frac{\partial E^{o}_{i}}{\partial M^{(r)}_{uv}} = \sum_s c^{(s)} \varepsilon^{o(s)}_{k} \frac{\partial B^{(s)}_{ki}}{\partial M^{(r)}_{uv}} \tag{B13}$$

Using (B5), we obtain:

$$\frac{\partial E_i^o}{\partial M_{uv}^{(r)}} = \zeta_{ikl}\frac{\partial \bar{M}_{kl}}{\partial M_{uv}^{(r)}} + \kappa_i^{(r,uv)} \tag{B14}$$

where:

$$\zeta_{ijk} = \sum_s c^{(s)} \varepsilon_m^{o(s)} \chi_{ml}^{(s)} \alpha_{lijk}^{(s)} \tag{B15}$$

$$\kappa_i^{(r,uv)} = -c^{(r)} \varepsilon_k^{o(r)} \chi_{ku}^{(r)} B_{vi}^{(r)} \tag{B16}$$

Calculation of $\partial \bar{G}/\partial M_{uv}^{(r)}$: Deriving equation (34):

$$\frac{\partial \bar{G}}{\partial M_{uv}^{(r)}} = \sum_s c^{(s)} \varepsilon_i^{o(s)} \frac{\partial b_i^{(s)}}{\partial M_{uv}^{(r)}} \tag{B17}$$

Deriving equation (18):

$$\frac{\partial b_i^{(s)}}{\partial M_{uv}^{(r)}} = -\chi_{iu}^{(s)} \delta_{rs} \chi_{vl}^{(s)} \left(E_l^o - \varepsilon_l^{o(s)}\right) - \chi^{(s)} \cdot \frac{\partial \tilde{M}}{\partial M_{uv}^{(r)}} \cdot \chi^{(s)} \cdot \left(E^o - \varepsilon^{o(s)}\right) + \chi^{(s)} \cdot \frac{\partial E^o}{\partial M_{uv}^{(r)}} \tag{B18}$$

Replacing (B17) in (B16) and using (B3):

$$\frac{\partial \bar{G}}{\partial M_{uv}^{(r)}} = \varphi_{ij} \frac{\partial M_{ij}^o}{\partial M_{uv}^{(r)}} + \vartheta_i \frac{\partial E_i^o}{\partial M_{uv}^{(r)}} + \eta^{(r,uv)} \tag{B19}$$

where:

$$\varphi_{ij} = -\left[\sum_s c^{(s)} \varepsilon_k^{o(s)} \chi_{kl}^{(s)} \chi_{pq}^{(s)} \left(E_q^o - \varepsilon_q^{o(s)}\right)\right] \theta_{lpij} \tag{B20}$$

$$\vartheta_i = \sum_s c^{(s)} \varepsilon_k^{o(s)} \chi_{ki}^{(s)} \tag{B21}$$

$$\eta^{(r,uv)} = -c^{(r)} \varepsilon_i^{o(r)} \chi_{iu}^{(r)} \chi_{vl}^{(r)} \left(E_l^o - \varepsilon_l^{o(r)}\right) \tag{B22}$$

Appendix C: Calculation of $\partial S/\partial \bar{M}$

The derivative of Eshelby tensor with respect to the effective compliance, appearing in (B4) can be obtained as follows. From equations (A14) and (A15) the (symmetric) Eshelby tensor of an ellipsoidal inclusion of radii (a, b, c) embedded in an

incompressible homogenous medium of stiffness $\bar{L} = \bar{M}^{-1}$ is given by (in tensor notation, all indices running from 1 to 3):

$$S_{ijmn} = T^{sym}_{ijkl} \bar{L}_{klmn} \tag{C1}$$

where:

$$T^{sym}_{ijkl} = \frac{abc}{16\pi} \int_0^{2\pi} \int_0^{\pi} \frac{\lambda_{ijkl}(\alpha)}{[\rho(\alpha)]^3} \sin\theta \, d\theta \, d\varphi \tag{C2}$$

with:

$$\lambda_{ijkl} = \alpha_j \alpha_l A^{-1}_{ik} + \alpha_i \alpha_l A^{-1}_{jk} + \alpha_j \alpha_k A^{-1}_{il} + \alpha_i \alpha_k A^{-1}_{jl} \tag{C3}$$

where the 4×4 matrix A is given by (A5). In particular:

$$A_{ik} = \bar{L}_{ijkl} \alpha_j \alpha_l \quad (i,j = 1,3) \tag{C4}$$

Deriving (C1):

$$\frac{\partial S_{ijmn}}{\partial \bar{M}} = \frac{\partial T^{sym}_{ijkl}}{\partial \bar{M}} \bar{L}_{klmn} + T^{sym}_{ijkl} \frac{\partial \bar{L}_{klmn}}{\partial \bar{M}} \tag{C5}$$

The first derivative on the right is obtained as:

$$\frac{\partial T_{ijkl}}{\partial \bar{M}} = \frac{abc}{16\pi} \int_0^{2\pi} \int_0^{\pi} \frac{\partial \lambda_{ijkl}}{\partial \bar{M}} \frac{\sin\theta \, d\theta \, d\varphi}{[\rho(\alpha)]^3} \tag{C6}$$

Using (C3) and (C4), $\partial \lambda_{ijkl} / \partial \bar{M}$ is calculated as:

$$\frac{\partial \lambda_{ijkl}}{\partial \bar{M}} = \alpha_j \alpha_l \frac{\partial A^{-1}_{ik}}{\partial \bar{M}} + \alpha_i \alpha_l \frac{\partial A^{-1}_{jk}}{\partial \bar{M}} + \alpha_j \alpha_k \frac{\partial A^{-1}_{il}}{\partial \bar{M}} + \alpha_i \alpha_k \frac{\partial A^{-1}_{jl}}{\partial \bar{M}} \tag{C7}$$

where

$$\frac{\partial A^{-1}_{ij}}{\partial \bar{M}} = -A^{-1}_{ik} \left(\frac{\partial \bar{L}_{klmn}}{\partial \bar{M}} \alpha_l \alpha_n \right) A^{-1}_{mj} \tag{C8}$$

The expression $\partial \bar{L}_{klmn} / \partial \bar{M}$ appearing in (C5) and (C8) is simply the derivative of a tensor with respect to its inverse. In matrix notation (indices running from 1 to 5):

$$\frac{\partial \bar{L}_{ij}}{\partial \bar{M}_{pq}} = -\frac{1}{2} \left(\bar{L}_{ip} \bar{L}_{qj} + \bar{L}_{iq} \bar{L}_{pj} \right) \tag{C9}$$

References

[1] A. Molinari, G.R. Canova and S. Ahzi, Acta Metall. **35** 2983 (1987).
[2] R.A. Lebensohn and C.N. Tomé, Acta Metall. Mater. **41** 2611 (1993).
[3] C.N. Tomé and R.A. Lebensohn, Manual for code viscoplastic self-consistent (*version* 7). Available at: http://public.lanl.gov/vpsc (accessed 9 March 2007).
[4] R.A. Lebensohn, P.V. Sanchez and A. Pochettino, Scripta Metall. Mater. **30** 481 (1994).
[5] H. Francillette, B. Bacroix, M. Gasperini, *et al.*, Acta Mater. **46** 4131 (1998).

[6] C.N. Tomé, P.J. Maudlin, R.A. Lebensohn, *et al*., Acta Mater. **49** 3085 (2001).
[7] G.C. Kaschner, C.N. Tomé, I.J. Beyerlein, *et al*., Acta Mater. **54** 2887 (2006).
[8] C. Maurice and J.H. Driver, Acta Mater. **45** 4639 (1997).
[9] A.B. Lopes, E.F. Rauch and J.J. Gracio, Acta Mater. **47** 859 (1999).
[10] O. Engler, M.Y. Huh and C.N. Tomé, Metall. Mater. Trans. A **31** 2299 (2000).
[11] C.N. Tomé, R.A. Lebensohn and C.T. Necker, Metall. Mater. Trans. A **33** 2635 (2002).
[12] F. Barlat, J.M.F. Duarte, J.J. Gracio, *et al*., Int. J. Plast. **19** 1215 (2003).
[13] O. Engler and S. Kalz, Mater. Sci. Eng. A **373** 350 (2004).
[14] R.A. Lebensohn and T. Leffers, Texture Microstruct. **31** 217 (1999).
[15] O. Engler, Acta Mater. **48** 4827 (2000).
[16] S.Y. Li, I.J. Beyerlein, C.T. Necker, *et al*., Acta Mater. **52** 4859 (2004).
[17] D. Dunst and H. Mecking, Z. Metallkd. **87** 498 (1996).
[18] R.A. Lebensohn and G.R. Canova, Acta Mater. **45** 3687 (1997).
[19] G.G. Yapici, I. Karaman and Z.P. Luo, Acta Mater. **54** 3755 (2006).
[20] S.B. Yi, H.G. Brokmeier, R.E. Bolmaro, *et al*., Scripta Mater. **51** 455 (2004).
[21] S.R. Agnew and O. Duygulu, Int. J. Plast. **21** 1161 (2005).
[22] R.H. Wagoner, X.Y. Lou, M. Li, *et al*., J. Mater. Process Technol. **177** 483 (2006).
[23] T. Walde and H. Riedel, Mater. Sci. Eng. A **443** 277 (2007).
[24] B. Bacroix, A. Miroux and O. Castelnau, Model. Simul. Mater. Sci. Eng. **7** 85 (1999).
[25] I. Karaman, H. Sehitoglu, A.J. Beaudoin, *et al*., Acta Mater. **48** 2031 (2000).
[26] O. Engler, M.Y. Huh and C.N. Tomé, Metall. Mater. Trans. A **36** 3127 (2005).
[27] D.A. Hughes, R.A. Lebensohn, H.-R. Wenk, *et al*., Proc. R. Soc. Lond. A **456** 921 (2000).
[28] R.A. Lebensohn and C.N. Tomé, Mater. Sci. Eng. A **175** 71 (1994).
[29] D.W. Brown, S.P. Abeln, W.R. Blumenthal, *et al*., Metall. Mater. Trans. A **36** 929 (2005).
[30] I.J. Beyerlein, L.S. Tóth, C.N. Tomé, *et al*., Phil. Mag. **87** 885 (2007).
[31] R. Lebensohn, Model. Simul. Mater. Sci. Eng. **7** 739 (1999).
[32] B. Commentz, C. Hartig and H. Mecking, Comp. Mater. Sci. **16** 237 (1999).
[33] A.U. Telang and T.R. Bieler, J. Metals **57** 44 (2005).
[34] K. Al-Fadhalah, C.N. Tomé, A.J. Beaudoin, *et al*., Phil. Mag. **85** 1419 (2005).
[35] O. Castelnau, P. Duval, R.A. Lebensohn, *et al*., J. Geophys. Res. B **101** 13851 (1996).
[36] K. Bennett, H.R. Wenk, W.B. Durham, *et al*., Phil. Mag. A **76** 413 (1997).
[37] O. Castelnau, H. Shoji, A. Mangeney, *et al*., Earth Planet Sci. Lett. **154** 307 (1998).
[38] R.A. Lebensohn, H.R. Wenk and C.N. Tomé, Acta Mater. **46** 2683 (1998).
[39] T. Takeshita, H.R. Wenk and R.A. Lebensohn, Tectonophysics **312** 133 (1999).
[40] R.A. Lebensohn, P.R. Dawson, H.M. Kern, *et al*., Tectonophysics **370** 287 (2003).
[41] H.R. Wenk, J. Baumgardner, R.A. Lebensohn, *et al*., J. Geophys. Res. B **105** 5663 (2000).
[42] H.R. Wenk, S. Matthies, R.J. Hemley, *et al*., Nature **405** 1044 (2000).
[43] A. Tommasi, Earth Planet Sci. Lett. **160** 1 (1998).
[44] H.R. Wenk and C.N. Tomé, J. Geophys. Res. B **104** 25513 (1999).
[45] D. Mainprice, A. Tommasi, H. Couvy, *et al*., Nature **433** 731 (2005).
[46] A. Tommasi, D. Mainprice, O. Cordier, *et al*., J. Geophys. Res. B **109** 12405 (2004).
[47] P. Carrez, P. Cordier, D. Mainprice, *et al*., Eur. J. Mineral. **18** 149 (2006).
[48] H.R. Wenk, G. Ischia, N. Nishiyama, *et al*., Phys. Earth Planet Int. **152** 191 (2005).
[49] H.R. Wenk, S. Speziale, A.K. McNamara, *et al*., Earth Planet Sci. Lett. **245** 302 (2006).
[50] S. Merkel, H.R. Wenk, J.F. Shu, *et al*., J. Geophys. Res. B **107** 2271 (2002).
[51] P. Cordier, D. Mainprice and J.L. Mosenfelder, Eur. J. Mineral **16** 387 (2004).
[52] S. Nikolov, R.A. Lebensohn and D. Raabe, J. Mech. Phys. Solids **54** 1350 (2006).
[53] G. Proust, C.N. Tomé and G.C. Kaschner, Acta Mater. **55** 2137 (2007).
[54] H.R. Wenk, G.R. Canova, Y. Brechet, *et al*., Acta Mater. **45** 3283 (1997).
[55] J.W. Signorelli, R. Logé, Y. Chastel, *et al*., Model. Simul. Mater. Sci. Eng. **8** 193 (2000).
[56] I.J. Beyerlein, R.A. Lebensohn and C.N. Tomé, Mater. Sci. Eng. A **345** 122 (2003).

[57] R.A. Lebensohn, C.N. Tomé and P.J. Maudlin, J. Mech. Phys. Solids **52** 249 (2004).
[58] B. Plunkett, R.A. Lebensohn, O. Cazacu, *et al.*, Acta Mater. **54** 4159 (2006).
[59] B. Plunkett, O. Cazacu, R.A. Lebensohn, *et al.*, Int. J. Plast. **23** 1001 (2007).
[60] G.R. Canova, H.R. Wenk and A. Molinari, Acta Metall. Mater. **40** 1519 (1992).
[61] D.E. Solas and C.N. Tomé, Int. J. Plast. **17** 737 (2001).
[62] A.V. Hershey, J. Appl. Mech. **21** 236 (1954).
[63] R. Hill, J. Mech. Phys. Solids **13** 89 (1965).
[64] J.W. Hutchinson, Proc. R. Soc. Lond. A **348** 101 (1976).
[65] R. Masson, M. Bornert, P. Suquet, *et al.*, J. Mech. Phys. Solids **48** 1203 (2000).
[66] P. Gilormini, in *IUTAM Symposium on Micromechanics of Plasticity and Damage of Multiphase Materials*, edited by A. Pineau and A. Zaoui (Kluwer, Dordrecht, 1996), pp. 67–74.
[67] P. Ponte Castañeda, J. Mech. Phys. Solids **39** 45 (1991).
[68] G. deBotton and P. Ponte Castañeda, Proc. R. Soc. Lond. A **448** 121 (1995).
[69] P. Ponte Castañeda, J. Mech. Phys. Solids **50** 737 (2002).
[70] Y. Liu and P. Ponte Castañeda, J. Mech. Phys. Solids **52** 467 (2004).
[71] M.V. Nebozhyn, P. Gilormini and P. Ponte Castañeda, J. Mech. Phys. Solids **49** 313 (2001).
[72] P. Gilormini, M.V. Nebozhyn and P. Ponte Castañeda, Acta Mater. **49** 329 (2001).
[73] Y. Liu, P. Gilormini and P. Ponte Castañeda, Acta Mater. **51** 5425 (2003).
[74] Y. Liu and P. Ponte Castañeda, J. Mech. Phys. Solids **52** 1175 (2004).
[75] Y. Liu, P. Gilormini and P. Ponte Castañeda, Tectonophysics **406** 179 (2005).
[76] R.A. Lebensohn, Y. Liu and P. Ponte Castañeda, Acta Mater. **52** 5347 (2004).
[77] R.A. Lebensohn, P.A. Turner, J.W. Signorelli, *et al.*, Model. Simul. Mater. Sci. Eng. **6** 447 (1998).
[78] T. Mura, *Micromechanics of Defects in Solids* (Martinus-Nijhoff, Dordrecht, 1987).
[79] L.J. Walpole, J. Mech. Phys. Solids **17** 235 (1969).
[80] A. Molinari and L.S. Tóth, Acta Metal. Mater. **42** 2453 (1994).
[81] C.N. Tomé, Model. Simul. Mater. Sci. Eng. **7** 723 (1999).
[82] N. Laws, J. Mech. Phys. Solids **21** 9 (1973).
[83] J.R. Willis, Adv. Appl. Mech. **21** 1 (1981).
[84] P. Lequeu, P. Gilormini, F. Montheillet, *et al.*, Acta Metall. **35** 439 (1987).
[85] C.N. Tomé, G.R. Canova, U.F. Kocks, *et al.*, Acta Metall. **32** 1637 (1994).
[86] J.C. Michel, H. Moulinec and P. Suquet, Comp. Model. Eng. Sci. **1** 9 (2000).
[87] R.A. Lebensohn, Acta Mater. **49** 2723 (2001).
[88] M.I. Idiart and P. Ponte Castañeda, Proc. R. Soc. Lond. A **463** 183 (2007).
[89] H. Moulinec and P. Suquet, Eur. J. Mech. A Solids **22** 751 (2003).
[90] S.L. Semiatin and T.R. Bieler, Acta Mater. **49** 3565 (2001).
[91] M.V. Nebozhyn, P. Gilormini and P. Ponte Castañeda, C.R. Acad. Sci. Paris II (b) **328** 11 (2000).
[92] T. Leffers and R.K. Ray, (2007) (To be published).
[93] T. Leffers and D. Juul Jensen, Texture Microstruct. **14/18** 933 (1991).
[94] T. Leffers, Phys. Status Solidi **25** 337 (1968).
[95] R.A. Lebensohn and T. Leffers, (2007) (To be published).
[96] H. Hu and S.R. Goodman, Trans. Metall. Soc. AIME **227** 627 (1963).
[97] O. Castelnau, R. Brenner and R.A. Lebensohn, Acta Mater. **54** 2745 (2006).
[98] M. Berveiller, O. Fassi-Fehri and A. Hihi, Int. J. Eng. Sci. **25** 691 (1987).